# Effect of spatial variability on stability and failure mechanisms of 3D slope using random limit equilibrium method

Hu, Lihang
Department of Civil and Environmental Engineering, Tokyo Institute of Technology

Takahashi, Akihiro
Department of Civil and Environmental Engineering, Tokyo Institute of Technology

Kasama, Kiyonobu
Department of Civil Engineering, Kyushu University



出版情報：Soils and Foundations. 62 (6), pp.101225-, 2022-12. Elsevier
バージョン：

HOSTED BY
ELSEVIER
Available online at www.sciencedirect.com
ScienceDirect
Soils and Foundations 62 (2022) 101225
www.elsevier.com/locate/sandf

Technical Paper

# Effect of spatial variability on stability and failure mechanisms of 3D slope using random limit equilibrium method

Lihang Hu [a], Akihiro Takahashi [a,*], Kiyonobu Kasama [b]

[a] Department of Civil and Environmental Engineering, Tokyo Institute of Technology, Tokyo, Japan
[b] Department of Civil Engineering, Kyushu University, Fukuoka, Japan[1]

Received 3 January 2022; received in revised form 18 August 2022; accepted 12 September 2022

**Abstract**

It is well known that soils are prone to spatial non-uniformity, which affects evaluations of slope stability and failure mechanisms. This paper presents a probabilistic slope stability evaluation, considering the 3D spatial variation in the soil properties, by the random limit equilibrium method (*RLEM*). Specifically, 3D random fields of cohesion $c$, friction angle $\phi$, and soil unit weight $\gamma$ are generated using a fast Fourier transform. The *RLEM* is applied to evaluate the effects of the 3D spatial variability of the soil properties on slope stability and failure mechanisms. A Monte Carlo simulation is used to interpret the slope reliability and variation in slope failure dimension. Based on the critical slip surface passing different portions of a slope (slope base, inclined face, and crest), four main failure mechanisms (two base failures and two face failures), and one additional failure mechanism (toe failure), are identified for spatially variable slopes, and the corresponding distributions of the stability number ($N_s$) and sliding volume ($V$) are investigated in detail. The results show that the large variation in the soil properties induces changes in the failure mechanisms, and a threshold of $c$-$\phi$ values is found for a shift from base failure to toe failure. Lastly, associated sensitivity studies are performed to explore the effects of the uncertainties of the input parameters on the uncertainty of the output. The results estimated by partial Spearman correlation coefficients show that cohesion has the greatest influence on the stability number, and that a positive influence of the unit weight, contributing to slope stability, is found for a base failure mechanism.


*Keywords:* 3D slope stability; Monte Carlo simulation; Failure mechanism; Spatial variability; Sensitivity analysis

## 1. Introduction

There are three primary sources of uncertainties in geotechnical engineering, namely, inherent variability, measurement errors, and transformation uncertainty. In addition to the spatial variability of the soil properties, the shear strength and unit weight are well known to be inherent in the nature of soils, along with geotechnical uncertainties, due to complex geological processing throughout their formation. Phoon and Kulhawy (1999) reported that most soil mechanics parameters can be treated as random variables characterized statistically by a normal or log-normal distribution, and that soil variability can be described by the coefficient of variation ($COV$) and the scale of fluctuation (referred to as the correlation length ($\theta$)). When uncertainties are quantified, a reliability analysis can be used, and the influence of the spatial variability of the soil properties on slope stability can be examined.

Peer review under responsibility of The Japanese Geotechnical Society.
* Corresponding author at: 502, Midorigaoka 1st Build, 2-12-1 Ookayama, Meguro-Ku, Tokyo 152-8552, Japan.
*E-mail addresses:* lihang.h.aa@m.titech.ac.jp (L. Hu), takahashi.a.al@m.titech.ac.jp (A. Takahashi).
[1] Formerly, Department of Civil and Environmental Engineering, Tokyo Institute of Technology, Tokyo, Japan.

https://doi.org/10.1016/j.sandf.2022.101225
0038-0806/

The uncertainty and spatial variability of the soil parameters for a two-dimensional slope have been analyzed in detail. Mellah et al. (2000) used the stochastic finite element method (*SFEM*) to evaluate the uncertainty of the soil parameters as it relates to the reliability of an earth dam. They found that, for the dam core, the standard deviations in vertical displacement and strain show maximum values. Low et al. (2007) developed a spreadsheet platform using a limit equilibrium method (*LEM*) and Monte Carlo simulation (*MCS*) to account for the horizontal spatial variation in the soil properties. Griffiths and Fenton (2004) used the random finite element method (*RFEM*) to calculate the probability of failure, considering the spatial variability. They found that the failure probability increases with the correlation length (i.e., reduced spatial variability) when the coefficient of variation in cohesion ($COV_c$) is smaller than 0.65, and that there is an opposite trend in failure probability when the $COV_c$ is larger than 0.65. Moreover, they noted that ignoring the spatial variation leads to the underestimation of the probability of failure when the mean $F_s$ for a spatially variable slope is below 1.12. Furthermore, Huang et al. (2013) and Kasama and Whittle (2015) developed the random field numerical limit analysis (*RFNLA*), for use together with a *MCS*, to evaluate the distribution of the stability number and the probability of failure.

There is no information on the third dimension (slope length) of a 2D slope, which represents a spatial average over that dimension. Hence, a 2D analysis implicates unconservative results from an optimistic scenario of the correlation condition or conservative results from the worst-case scenario when compared with a 3D analysis. To tackle the slope probabilistic analysis in 3D, Vanmarcke (1977) firstly evaluated the 3D slope stability within a probabilistic framework, using a simplified 3D *LEM*. He pioneered the use of the mean $F_s$ through the first order second moment (*FOSM*) method and investigated the failure probability for a cylindrical failure mechanism. It has only been in recent years, and with the help of an improved numerical method and greater computational capacity, that the 3D problem has been studied in detail (Hicks et al., 2008; Griffiths et al., 2009; Hicks and Spencer, 2010; Hicks et al., 2014; Varkey et al., 2017). In particular, Hicks et al. (2008) and Hicks and Spencer (2010) explored the long slope (long length in the third dimension) stability under the influence of the anisotropic correlation length of undrained shear strength using the 3D *RFEM*. They discovered that a discrete failure mechanism is typical for a long slope with an intermediate level for the anisotropic correlation length. However, as later discussed by Hicks and Spencer (2010), an analysis for a short or representative slope section is also useful and can be applied for a long slope reliability assessment by means of the basic probability theory.

In addition to the failure probability and factor of safety, the area or volume of a sliding mass is also an important index that is widely used as a measure of failure consequence in risk assessments (Huang et al., 2013; Kasama et al., 2021b). Kasama and Whittle (2015) used random limit analyses to evaluate the 2D slope failure dimension for the failure depth and width. They suggested that increasing the spatial variability results in a decrease in the dimension of the slope failure, but an increase in the variability of the dimension. Hicks et al. (2008) used both the 2D *RFEM* and the 3D *RFEM* to evaluate 2D and 3D problems. They stated that there was no obvious link between the probability of failure and the slide volume and area, but that a trend of higher $F_s$ accompanying a smaller volume was observed. Although valuable attempts were made in the above studies to evaluate the failure mechanism for 2D and 3D spatially variable slopes, by assessing the dimension of a collapsed slope, a clear understanding and discussion of the slope failure dimension, such as the failure mechanism and sliding volume, are still needed. Moreover, the relationship between the factor of safety and the sliding volume, in terms of failure mechanisms, has rarely been studied, although it is important and effective to assess the effect of spatial variability on slope stability. Firstly, this study presents a probabilistic analysis for a 3D slope; a random limit equilibrium method is used in tandem with an *MCS* framework. Then, the relationship between the stability number and the sliding volume is investigated in detail in terms of the identified failure mechanisms. Lastly, a sensitivity analysis is conducted to improve the understanding of the effect of the spatially variable soil properties on the stability number, considering various failure mechanisms and using a partial Spearman correlation coefficient and the simplified Bishop method under the Mohr-Coulomb failure criterion.

## 2. Random limit equilibrium method

### 2.1. Limit equilibrium method (LEM)

A 2D *LEM* is often used in slope stability analyses because of its simplicity and reduced computational time. Bishop's simplified method (Bishop, 1955) and Janbu's simplified method (Janbu et al., 1956) are two frequently applied types of *LEM*. Using these methods, a soil mass is discretized into vertical slices, and the forces, moments, or stresses resisting the movement of the mass within the slices are evaluated. To facilitate the 3D analysis, Hungr (1987) proposed a 3D *LEM* based on the Bishop and Morgenstern–Price 2D *LEM*s by substituting rectangular columns for the vertical slices.

Although the *FEM* is regarded as a superior method, as it provides more detailed information on the stress–strain distribution and failure development (Naylor, 1982), the factor of safety and the locations of the critical failure surfaces obtained by the *LEM* and *FEM* agreed well in the deterministic slope stability analyses conducted by Chen et al. (2007), Liu et al. (2015), and Li et al. (2016). A detailed comparison was made between the *LEM* and the *FEM* by Matthews et al. (2014), who stated that the meth-

ods closely agree with each other, given a circular slip surface for a slope model without complex geometries or multiple layers. Considering a probabilistic slope stability analysis, Cho (2009) reported that the failure surfaces determined by the *RFEM* are similar to the critical circular surfaces determined by the *RLEM* and suggested that, only if the anisotropic spatial correlation is incorporated and the slope becomes stratified, a search for the critical non-circular surface is then required. Moreover, Lee and Ching (2020) validated the performance of the 3D *RLEM* by comparing it with a 3D *RFEM* performed on a 3D long slope. The results showed that the two methods produce a consistent factor of safety, sliding length, and sliding volume. As the slopes considered in the current paper incorporate the isotropic correlation length, to be demonstrated later, it is expected that the output from the 3D *RLEM* should be consistent with that from the 3D *RFEM*. Another advantage of *LEM* is its significantly computational efficiency, which ensures that a statistical interpretation by an *MCS* can be carried out for the 3D slope stability analysis. It is important to note, however, that the employed *RLEM*, the method using columns (simplified Bishop), requires prior assumptions of the column side force and a spherical failure mechanism, which are not required with the *RFEM*/*RFDM* as the failure occurs naturally over the zone in which the failure criterion is violated. Consequently, larger values for the variation in the stability number (factor of safety) and sliding volume will be obtained, and progressive failures can be monitored if the *RFEM*/*RFDM* is employed.

In this study, a 3D *LEM* is used along with Scoops3D (Reid et al., 2015), a software program that evaluates slope stability using a digital landscape represented by a digital elevation model (*DEM*). Scoops3D uses a simplified Bishop's method in 3D, and its solutions are assumed by the spherical trial surface with a global minimum *FS*. In addition, a flow chart of the *RLEM* used in this study is illustrated in Fig. 1. Firstly, three 3D slope models with different angles are built by *DEM*, and the random fields for the soil properties ($c$, $\tan\phi$, and $\gamma$) are generated according to the prescribed statistical information. Then, an *MCS* is performed to generate 1000 sets of random fields, and the *DEM* and the random fields of the soil properties are fed into Scoops3D to estimate the $F_s$, $V$, and critical slip surface. Next, the statistics are calculated for $F_s$ and $V$ (i.e., mean, standard deviation, COV of $F_s$, and $V$), and the failure mechanism is identified using the critical slip surfaces. Finally, the input information is changed for random fields, and a new round of simulations is started.

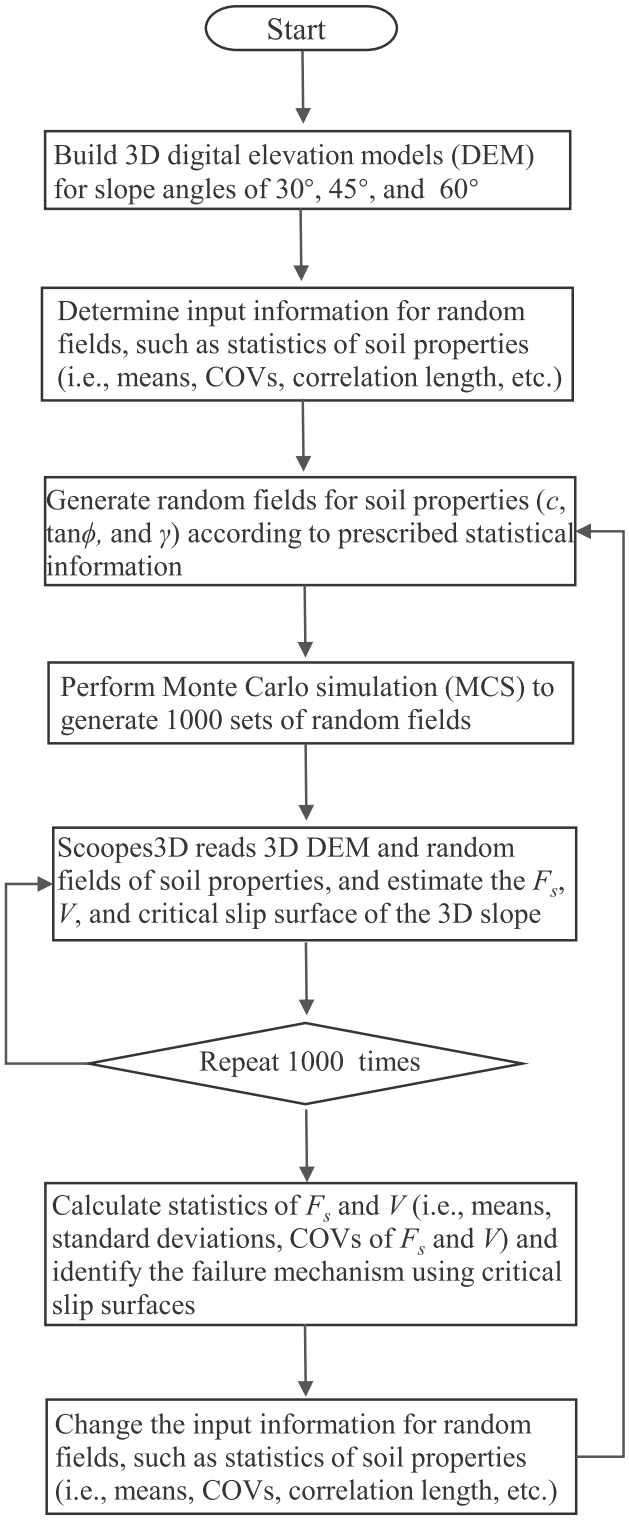


Fig. 1. Flow chart for random limit equilibrium method (*RLEM*).

## 2.2. Random field model

Guided by Vanmarcke (1977), the spatial variability of the soil properties, such as cohesion $c$, shear strength $\tan\phi$, and soil unit weight $\gamma$, are modeled in this study as the isotropic random field. The shear strength and soil unit weight are assumed to have an underlying log-normal distribution to ensure the non-negative properties, with mean averages of $\mu_{\ln\ \tan\phi}$, $\mu_{\ln c}$, and $\mu_{\ln\gamma}$, and standard deviations of $\sigma_{\ln\ \tan\phi}$, $\sigma_{\ln c}$, and $\sigma_{\ln\gamma}$. The dimensionless *COV* parameter is expressed as the ratio of the standard deviation ($\sigma$) with respect to the mean value ($\mu$), as given in Eq. (1).

$$COV = \frac{\sigma}{\mu} \tag{1}$$

The random fields of the shear strength and soil unit weight are assigned an approximately log-normal distribution. The mean and standard deviations are obtained as follows:

$$\mu_{\ln\tan\phi} = \ln\mu_{\tan\phi} - \frac{1}{2}\sigma^2_{\ln\tan\phi} \quad \sigma_{\ln\tan\phi} = \sqrt{\ln\left(1 + COV^2_{\tan\phi}\right)} \tag{2}$$

$$\mu_{\ln c} = \ln\mu_c - \frac{1}{2}\sigma^2_{\ln c} \quad \sigma_{\ln c} = \sqrt{\ln\left(1 + COV^2_c\right)} \tag{3}$$

$$R = \sigma_{N_s\_\text{single}} \,/\sigma_{N_s\_\text{three}} \tag{4}$$

The spatial variables of cohesion $c$, soil shear strength $\tan\phi$, and unit weight $\gamma$, for the $i$th element, are transformed from the standard normal Gaussian variables as follows:

$$c_i = \exp\left(\mu_{\ln c} + \sigma_{\ln c} \cdot G_i\right) \tag{5}$$

$$\tan\phi_i = \exp\left(\mu_{\ln\tan_\phi} + \sigma_{\ln\tan_\phi} \cdot G_i\right) \tag{6}$$

$$\gamma_i = \exp\left(\mu_{\ln_\gamma} + \sigma_{\ln_\gamma} \cdot G_i\right) \tag{7}$$

where $G_i$ is a standard Gaussian random variable that is linked to correlation length $\theta$. This study used the fast Fourier transform technique to generate $G_i$ from isotropic random field $G$ with a mean of zero and standard deviation of one (a standard normal distribution). Li et al. (2015) investigated the influence of five theoretical correlation functions on slope stability and reported that slope stability is not sensitive to the type of correlation function. Hence, the most popular function, the exponential Gauss–Markov correlation function, is adopted here as follows:

$$\rho = \exp\left(-\frac{2\sqrt{\left(x_i - x_j\right)^2 + \left(y_i - y_j\right)^2 + \left(z_i - z_j\right)^2}}{\theta}\right) \tag{8}$$

where $\rho$ is the correlation function, $x$, $y$, and $z$ are the directions of the three coordinates, and $x_i$-$x_j$, $y_i$-$y_j$, and $z_i$-$z_j$ are the lag distances. Similarly, $\theta$ is the correlation length.

Table 1 summarizes all the input parameters. Slope angles of $\beta = 30°$, 45°, and 60° are chosen as three typical slope inclinations, to facilitate the evaluation of the angle effects on slope stability and the failure mechanisms. The mean values of the shear strength parameters, cohesion $\mu_c = 100$ kPa and friction angle $\mu_\phi = 30°$, are mainly used for the analysis. These values are referred to as the shear strength parameters for soil-rock mixtures. It was reported by Zhang et al. (2019) that cohesion of 100 kPa with a friction angle of 30° is found in a soil-rock mixture with a 40 % rock block proportion. Hence, this soil-rock mixture is taken as the investigated ground in the current analysis, as it is the type of mixture often found in mountainous areas. Other types of soil, together with possible combinations of shear strength parameters, are investigated in the final subsection. As for the $COV$ of the soil properties, the $COV$ of the unit weight ($COV_\gamma$), fixed at 0.1 as the typical $COV_\gamma$, is small and no more than 10 % in measurement (Phoon and Kulhawy, 1999). In order to evaluate the influence of the $COV_s$ of cohesion ($COV_c$) and the internal friction angle ($COV_{\tan\phi}$) on slope stability, this study considers $COV_c$ and $COV_{\tan\phi}$ values in the ranges of 0.2 to 1.0 and 0.1 to 0.5, respectively. These values are higher than those reported in the literature, where $COV_c$ and $COV_{\tan\phi}$ are typically in the ranges of 0.1 to 0.5 and 0.05 to 0.2, respectively (Lee and Ching, 2020; Phoon and Kulhawy, 1999). Certain combinations of $COV_c$ and $COV_{\tan\phi}$ are considered, such as 0.2 and 0.1, respectively, and 1.0 and 0.5, respectively. These combinations accommodate the same order of increase or decrease in the $COV$ of the shear strength. And, for a simple demonstration, $COV_s$ is used to represent $COV_c$ and $COV_{\tan\phi}$. The random field in this study is assumed to be isotropic, with the same correlation length in three directions and a similar correlation length of the soil property $\theta = \theta_{\ln\ \tan\phi} = \theta_{\ln c} = \theta_{\ln\gamma}$. This isotropic correlation structure also improves the confidence of using a circular (spherical) search mechanism (Cho, 2009). Following Kasama and Whittle (2015), this study introduces the ratio between the correlation length and the slope height, $\Theta = \theta_{\ln\tan\phi}/H = \theta_{\ln c}/H = \theta_{\ln\gamma}/H$, as an input parameter, and $\Theta$ falls in the range of 0.05 to 1.0. This range in $\Theta$ is equivalent to $\theta = 1$ to 20 m, considering the slope model under study for a cell size of 1 m, width and length of 100 m, and height of 20 m. For the $c$-$\phi$ soil slope model considered in this study, the dependence between the strength parameters, i.e., the cross-correlation between the cohesive and friction angle $\rho_{c\text{-}\tan\phi}$, is needed. As for the cross-correlation between cohesion and the friction angle, Hassan and Wolff (1999) and Rahardjo et al. (2012) reported both positive and negative cross-correlations, while El-Ramly et al. (2006) and Suchomel and Mašin (2010) reported that there is no cross-correlation based on their experimental results. In addition, Wu (2015) summarized that the cross-correlation lies in the range of −0.78 to 0.37 based on an extensive literature review covering 391 soil samples. Therefore, following Chen et al. (2022), this study assumes a slightly positive and negative cross-correlation coefficient between $c$ and $\phi$ ($\rho_{c\text{-}\tan\phi} = 0.5$ and −0.5). The influence of the cross-correlation coefficient on the slope reliability will be discussed further using Fig. 9, and the results for $\rho_{c\text{-}\tan\phi} = 0.5$ are mainly explained in this paper. As for the cross-correlation between the shear strength and the unit weight, there has been no adequate study on them. However, some positive results have been reported from laboratory measurements (Matsuo and Kuroda 1974; Parker et al. 2008). In literature, positive cross-correlations for these random variables are most often assumed (Chowdhury and Xu 1993; Sivakumar and Srivastava 2007). Hence, following the same assumption, a positive cross-correlation between the shear strength and the unit weight is assumed, $\rho_{\gamma\text{-}c} = 1.0$ and $\rho_{\gamma\text{-}\tan\phi} = 1.0$.

Table 1
Input parameters.

| Parameter | Value |
|---|---|
| Angle of slope, $\beta$ | 30°, 45° & 60° |
| Mean soil cohesion, $\mu_c$ | 100 kPa |
| *COV* of cohesion, $COV_c$ | 0.2, 0.4, 0.6, 0.8 and 1.0 |
| Mean friction angle, $\mu_{\tan\phi}$ | 0.5774 ($\mu_\phi = 30°$) |
| *COV* of friction angle, $COV_{\tan\phi}$ | 0.1, 0.2, 0.3, 0.4 and 0.5 |
| Mean unit weight, $\mu_\gamma$ | 20 kN/m$^3$ |
| *COV* of unit weight, $COV_\gamma$ | 0.1 |
| Ratio of vertical and horizontal correlation length | 1 (Isotropic) |
| Normalized correlation length, $\Theta = \theta_{\ln\tan\phi} / H = \theta_{\ln c} / H = \theta_{\ln\gamma} / H$ | Random, 0.05, 0.25, 0.5 and 1.0 |
| Cross-correlation coefficient between $c$, $\tan\phi$, and $\gamma$ | $\rho_{c\text{-}\tan\phi} = 0.5$, $\rho_{\gamma\text{-}c} = 1.0$ and $\rho_{\gamma\text{-}\tan\phi} = 1.0$ |
| Monte Carlo iteration | 1000 |

*COV*: Coefficient of variation.

Finally, 1000 iterations of the *MCS* are conducted to accommodate the statistic interpretation of the stability analysis.

Fig. 2 shows a sample *DEM* slope for one realization, with given conditions of $\Theta = 1.0$ and $COV_c = 0.2$. There is a soil base layer of depth $d/H = 1.0$, horizontal length $l/H = 5.0$, and width $w/H = 5.0$, where $H$ is the height of the slope. The figure illustrates the spatial distribution of soil cohesion for each cubic element at a resolution of 1.0 m, as one realization with the input parameter of $\mu_c = 100$ kPa and an isotropic correlation length of $\Theta_x = \Theta_y = \Theta_z$. The red and blue regions indicate strong and weak soil strengths, respectively.

## 3. Analysis results

Table 2 summarizes the statistics for a stability number $N_s$ and sliding volume $V$ where the slope angle = 30°. The results for slope angles of 45° and 60° are summarized in Appendices 1 and 2. It is noted that $D_n$ is the test statistic proposed by Fenton and Griffiths (2008) for a normality test using the Kolmogorov–Smirnov method, which indicates the difference between the tested data and a fitted distribution, as shown in Eq. (9). Before comparing Dn to the acceptance criterion, an adjusted factor is used for Dn for different distributions. The adjusted versions of Dn for a normal (lognormal) distribution are shown by Eq. (10). The bold italic values for Dn,adj in Table 2 and Appendices 1 and 2 indicate that there is no fit.

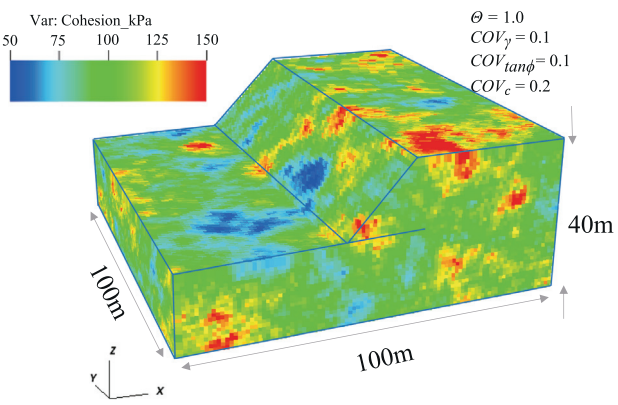


Fig. 2. Slope geometry and example of spatial variability.

$$D_n = \max_x \left| \widehat{F}(x) - F(x) \right| \tag{9}$$

where $\widehat{F}(x)$ is the CDF of the fitted distribution and F(x) is the empirical distribution function of the tested data.

$$D_{n,adj} = \left( \sqrt{n} - 0.01 + \frac{0.85}{\sqrt{n}} \right) D_n \tag{10}$$

where $D_{n,adj}$ is the adjusted version of test statistic D*n* and n is the total number of samples.

### 3.1. Stability number

Stability number $N_s$, proposed by Yu et al. (1998), is used to evaluate the stochastic property of slope stability with the spatial variability of the soil properties. The computed stability number for a slope is reported for each random field $i$ of the MCS $N_{si}$, as follows:

$$N_{si} = \frac{F_{si} \cdot \mu_\gamma \cdot H}{\mu_c} \tag{11}$$

where $N_{si}$ is the stability number for the $i$th random field and $F_{si}$ is the factor of safety of the slope for the $i$th random field. It is noted that $N_{si}$ is a direct proportional linear function of $F_{si}$; a large stability number means a slope with a large factor of safety. Unlike $F_s$, $N_s$ contains more detailed information on slope height $H$, the factor of safety of a homogeneous slope $F_{s\_hom}$, the mean value of cohesion $\mu_c$, and unit weight $\mu_\gamma$, which can also be regarded as consideration of normalization. Another important reason for using the stability number is that the factors of safety estimated in this study are all larger than 1.0, and an evaluation of such large values provides less information.

In order to evaluate the effect of spatial variability in terms of each set of *MCS*, a mean stability number, $\mu_{N_s}$, and its standard deviation, $\sigma_{N_s}$, are introduced.

$$\mu_{Ns} = \frac{1}{n} \sum_1^n N_{si} \; \sigma_{N_s} = \sqrt{\frac{1}{n-1} \sum_1^n \left( N_{si} - \mu_{N_s} \right)^2} \tag{12}$$

where $\mu_{N_s}$ is the mean of stability number $N_s$, $N_{si}$ is the estimated stability number for each Monte Carlo trial (each random field), and $n$ is the number of Monte Carlo trials.

The cumulative mean and *COV* of $N_s$ in the *MCS* for trial number $n = 1000$, $\Theta = 1.0$, $COV_\gamma = 0.1$, and $COV_s = 0.2$ and 0.1, 0.6 and 0.3, and 1.0 and 0.5, are plotted in Fig. 3 (a) and (b), respectively. Fig. 3 (a) shows that $\mu_{N_s}$ reaches a stable value within 1000 trials of the *MCS*, and Fig. 3 (b) shows that the cumulative *COV* of stability number $COV_{Ns}$ becomes stable within 1000 iterations. Thus, it is suggested that the 1000 iterations of the *MCS* conducted in this study are sufficient to obtain an accurate

Table 2
Stability number, sliding volume, and g/Goodness-of-fit results for normal and log-normal distributions of $\beta = 30°$.

| $\Theta$ | $COV_c$ & $_{\tan\phi}$ | $\mu_{Ns}$ | $\beta = 30°$ | | | | | | | | $\mu_{\ln(V)}$ | $\sigma_{\ln(V)}$ | $D_{n,\mathrm{adj}}$ |
|---|---|---|---|---|---|---|---|---|---|---|---|---|---|
| | | | $\sigma_{Ns}$ | $D_{n,\mathrm{adj}}$ | $\mu_{\ln(Ns)}$ | $\sigma_{\ln(Ns)}$ | $D_{n,\mathrm{adj}}$ | $\mu_V$ (m$^3$) | $\sigma_V$ (m$^3$) | $D_{n,\mathrm{adj}}$ | | | |
| Random | 0.2 & 0.1 | 14.81 | 0.02 | 0.661 | 2.69 | 0.0015 | 0.8550 | 20147.62 | 1263.39 | 0.928 | 9.90 | 0.0627 | 0.7046 |
| | 0.4 & 0.2 | 14.70 | 0.04 | 0.5325 | 2.69 | 0.0031 | 0.7327 | 19727.35 | 1898.29 | 0.6372 | 9.89 | 0.0967 | 0.7098 |
| | 0.6 & 0.3 | 14.57 | 0.07 | 0.6771 | 2.68 | 0.0048 | 0.7556 | 19296.89 | 2351.45 | 0.6581 | 9.86 | 0.1223 | 0.7976 |
| | 0.8 & 0.4 | 14.43 | 0.10 | 0.5501 | 2.67 | 0.0067 | 0.9510 | 18825.08 | 2623.13 | 0.7688 | 9.83 | 0.1404 | 0.6998 |
| | 1.0 & 0.5 | 14.28 | 0.12 | 0.5998 | 2.66 | 0.0086 | 0.9097 | 18486.44 | 2848.43 | 0.8100 | 9.81 | 0.1551 | 0.7481 |
| 0.01 | 0.2 & 0.1 | 14.78 | 0.03 | 0.8226 | 2.69 | 0.0023 | 0.8224 | 20054.81 | 1754.56 | 0.8712 | 9.90 | 0.0880 | 0.5960 |
| | 0.4 & 0.2 | 14.65 | 0.06 | 0.7848 | 2.68 | 0.0043 | 0.6318 | 19715.32 | 2559.46 | 0.7012 | 9.88 | 0.1294 | 0.6193 |
| | 0.6 & 0.3 | 14.49 | 0.09 | 0.7571 | 2.67 | 0.0064 | 0.6230 | 19134.96 | 2953.36 | 0.7625 | 9.85 | 0.1531 | 0.4161 |
| | 0.8 & 0.4 | 14.33 | 0.12 | 0.8290 | 2.66 | 0.0087 | 0.7688 | 18747.02 | 3327.86 | 0.9302 | 9.82 | 0.1767 | 0.5227 |
| | 1.0 & 0.5 | 14.16 | 0.16 | 0.8349 | 2.65 | 0.0110 | 0.5459 | 17423.75 | 4844.71 | 0.9421 | 9.80 | 0.1895 | 0.3167 |
| 0.25 | 0.2 & 0.1 | 14.53 | 0.25 | 0.7914 | 2.68 | 0.0173 | 0.8302 | 19194.26 | 3341.59 | 0.8941 | 9.85 | 0.1702 | 0.4135 |
| | 0.4 & 0.2 | 14.26 | 0.32 | 0.6730 | 2.66 | 0.0222 | 0.6961 | 18545.56 | 4565.00 | 0.9762 | 9.80 | 0.2454 | 0.3894 |
| | 0.6 & 0.3 | 13.85 | 0.46 | 0.5221 | 2.63 | 0.0330 | 0.5732 | 17706.12 | 5791.35 | 1.0009 | 9.73 | 0.3135 | 0.4058 |
| | 0.8 & 0.4 | 13.42 | 0.58 | 0.6635 | 2.60 | 0.0433 | 0.5893 | 16620.05 | 6659.15 | ***1.5377*** | 9.64 | 0.4093 | 0.6455 |
| | 1.0 & 0.5 | 11.98 | 0.71 | 0.5695 | 2.56 | 0.0562 | 0.5850 | 15762.95 | 7585.94 | ***1.4997*** | 9.53 | 0.6000 | 0.3167 |
| 0.50 | 0.2 & 0.1 | 14.47 | 0.33 | 0.6771 | 2.67 | 0.0231 | 0.7003 | 19158.55 | 3511.84 | 0.8869 | 9.84 | 0.1789 | 0.4080 |
| | 0.4 & 0.2 | 13.98 | 0.62 | 0.5664 | 2.64 | 0.0445 | 0.3981 | 18148.66 | 5640.15 | ***1.2662*** | 9.76 | 0.3099 | 0.4663 |
| | 0.6 & 0.3 | 13.38 | 0.92 | 0.4145 | 2.59 | 0.0685 | 0.3771 | 16618.08 | 7632.27 | 0.9957 | 9.61 | 0.4985 | 0.6532 |
| | 0.8 & 0.4 | 12.65 | 1.22 | 0.5315 | 2.53 | 0.0976 | 0.6162 | 13920.93 | 9328.36 | ***2.1642*** | 9.24 | 0.9590 | ***2.9235*** |
| | 1.0 & 0.5 | 11.64 | 1.50 | 0.6613 | 2.45 | 0.1328 | 0.9202 | 10802.15 | 10203.83 | ***4.6320*** | 8.60 | 1.4830 | ***4.5990*** |
| 1.0 | 0.2 & 0.1 | 14.35 | 0.54 | 0.5822 | 2.66 | 0.0376 | 0.7613 | 18724.15 | 3700.85 | ***1.0853*** | 9.82 | 0.1921 | 0.5259 |
| | 0.4 & 0.2 | 13.63 | 1.08 | 0.8100 | 2.61 | 0.0802 | 0.6491 | 17023.05 | 6676.11 | ***1.2072*** | 9.67 | 0.3797 | 0.6817 |
| | 0.6 & 0.3 | 12.75 | 1.54 | 0.5632 | 2.54 | 0.1232 | 0.6796 | 15231.93 | 10166.19 | ***1.3510*** | 9.11 | 0.7521 | 0.9947 |
| | 0.8 & 0.4 | 11.66 | 1.99 | 0.9239 | 2.44 | 0.1732 | 0.4526 | 11408.69 | 10697.34 | ***4.5574*** | 8.82 | 1.2174 | ***2.9136*** |
| | 1.0 & 0.5 | 10.18 | 2.24 | 0.9429 | 2.30 | 0.2298 | 0.6320 | 7659.88 | 10421.30 | ***7.3404*** | 7.96 | 1.6214 | ***2.0841*** |

Note: Acceptance criterion $D_{\mathrm{n},\alpha,}[1000, 0.01] \leq 1.035$.

and reliable evaluation of $N_s$. It is noteworthy that the smaller the $COV_s$ is, the fewer iterations of *MCS* are required.

Fig. 4 depicts histograms of the $N_s$ from three complete series of *MCS*, with $COV_s$ = 1.0 and 0.5, 0.6 and 0.3, and 0.2 and 0.1, for given normalized correlation lengths of $\Theta = 0.25$ and 1.0 and a slope angle of 30°. The solid curves in Fig. 4 (a) are the estimated normal fits. In general, the $N_s$ values for spatially variable slopes are smaller than those for homogeneous slopes, indicating that spatial variability tends to cause instability. The histogram distribution shows that $COV_{Ns}$ increases with an increasing *COV* of shear strength ($COV_s$), indicating that large $COV_s$ leads to a large variation in $N_s$, and results in a more uniform distribution pattern. The solid curves in Fig. 4 (b) are the estimated log-normal fits. It is seen that a log-normal distribution can also be used to feature the stability number. However, it should be noted that the *COV* of the stability number in Fig. 4 (b) for $\Theta = 1.0$ is larger than that in Fig. 4 (a) for $\Theta = 0.25$, which suggests that a large $\Theta$ also leads to a large variation in distribution. In addition, to obtain the distribution function of the stability number, Table 2 summarizes the statistics of the Kolmogorov–Smirnov (*K-S*) test for all simulations of slope angle $\beta = 30°$. (The results of $\beta = 45°$ and $\beta = 60°$ are summarized in Appendices 1 and 2.) It is confirmed that normal and log-normal distribution functions can be sensible choices of fit for the stability number at a 1 % significance level, with an acceptance criterion of $D_{1000,\mathrm{adj}} < D_{n,\alpha}$ [1000, 0.01] = 1.032.

Fig. 5 presents the relationships between the mean stability number $\mu_{\mathrm{Ns}}$ for $\Theta = 1.0$ and the slope angle. In order to compare the results with the literature, the stability number for homogeneous strength from Ugai and Hosobori (1988) is also plotted, as a broken red line. The results for $COV_{\tan\phi} = 0$ and $COV_c = 0$ ($COV_s = 0$) indicate a slope with homogeneous strength. It is seen that the stability numbers obtained by this study for a homogeneous slope $N_{s\_\mathrm{hom}}$ with slope angles of 30°, 45°, and 60° are 14.85, 12.09, and 9.42, respectively. This is comparable to the results reported by Ugai and Hosobori (1988), with only a 2 % difference for $\beta = 30°$ and 45°, and a 4 % difference for $\beta = 60°$. These comparable results confirm the reliability of Scoops3D. In addition to the effect of slope angle, it is evident that a steep slope results in a small stability number, for both homogeneous and spatially variable slopes.

Fig. 6 summarizes the coefficient of variation in stability number for all the input spatial variability conditions, for a slope angle of $\beta = 45°$. Within the studied range of spatial variability (0 to 1.0 for $COV_s$ and random to 1.0 for $\Theta$), for a given $\Theta$ increases linearly with increasing $COV_s$, and the rate of increase in $COV_{Ns}$ increases as $\Theta$ increases from random to 1.0. Moreover, as introduced by El-Ramly et al. (2002), slope stability is more likely to be controlled

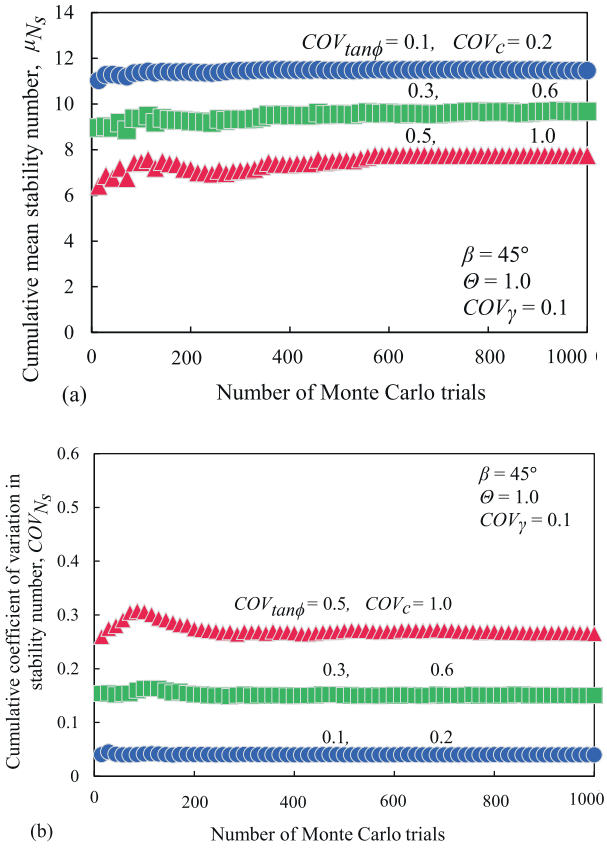


Fig. 3. Cumulative mean and coefficient of variation in stability number in Monte Carlo trials: (a) cumulative mean stability number and (b) cumulative coefficient of variation in stability number.

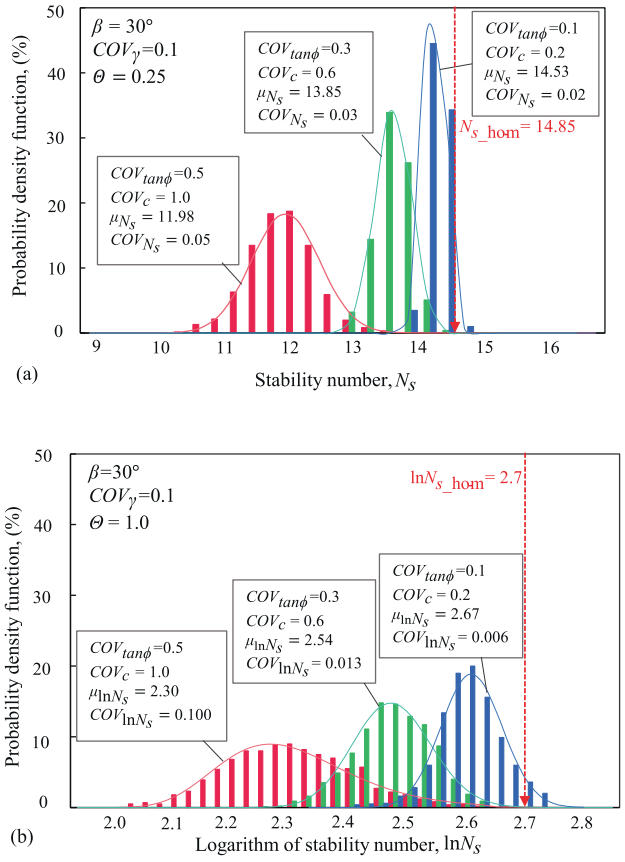


Fig. 4. Probability density function of stability number: (a) normal distribution and (b) log-normal distribution.

by the average soil properties, that is, the uncertainty of the average strength along a slip surface. The effects of such strength averaging can be observed when $COV_{Ns}$ is relatively small (maximum 0.27), and even when $COV_s$ is large ($COV_s$ = 1.0 and 0.5), suggesting that the variability of strength averages locally along the slip surface of a slope.

Spatial variability leads to a reduction in the stability number, as shown in Fig. 5. Thus, in order to evaluate the reduction effect of the stability number, irrespective of the slope angle, the stability number ratio $R_{Ns}$ and its mean $\mu_{R_{Ns}}$ are proposed.

$$R_{Nsi} = \frac{N_{si}}{N_{s\_hom}} \quad \mu_{R_{Ns}} = \frac{1}{n}\sum_{1}^{n} R_{si} \tag{13}$$

For creating safer slope designs, it is sensible to consider lower stability numbers (or factors of safety). Fig. 7 does so; and thus, the 99 % lower confidence bound of the stability number ratio for the input spatial variability is demonstrated. According to Eq. (11), the 99 % lower confidence bound of the stability number ratio is $R_{Ns99\%} = N_{s99\%}/N_{s\_hom}$, where $N_{s99\%}$ is estimated by assuming a log-normal distribution with $\mu_{\ln Ns}$ and $\sigma_{\ln Ns}$. In general, $R_{Ns} < 1$. Hence, spatial variability causes a reduction in the expected slope stability. The largest reductions in $\mu_{R_{Ns}}$ occur when the $COV$ is high and/or the correlation length

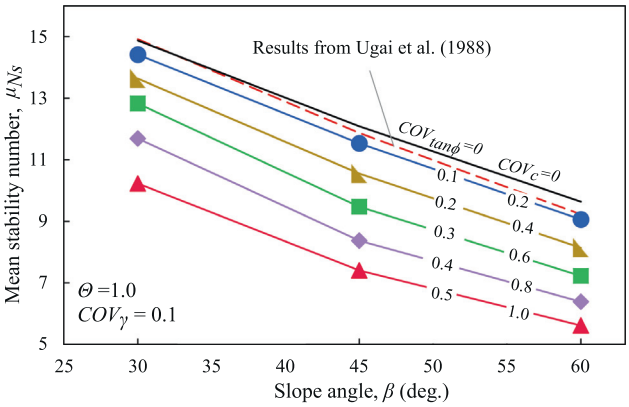


Fig. 5. Mean stability number against slope angle.

is large. For instance, the maximum decrease in $\mu_{R_{Ns}}$ is 14 %, when $\Theta$ varies from 0.05 to 0.25 and when $COV_s$ = 1.0. Specifically, the 99 % lower confidence bound of the stability number ratio shows a minimum value for $COV_s$ = 1.0 and 0.5. However, this observation of the stability number decreasing with increasing isotropic correlation is not in agreement with the observations of researchers such as Kasama and Whittle (2015) and Tabarroki et al. (2013), who found that the stability number (factor of safety) first decreases at small correlation lengths and then recovers when the correlation length grad-

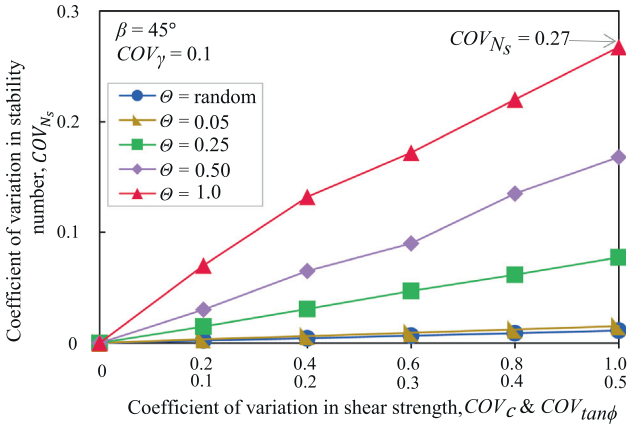


Fig. 6. Influence of spatial variability of shear strength on *COV* of stability number.

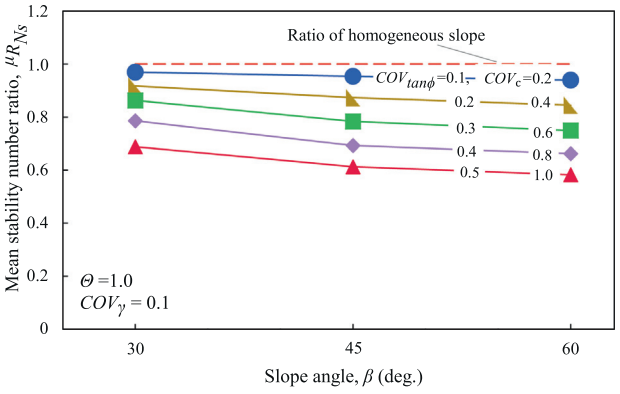


Fig. 8. Mean stability number ratio against slope angle.

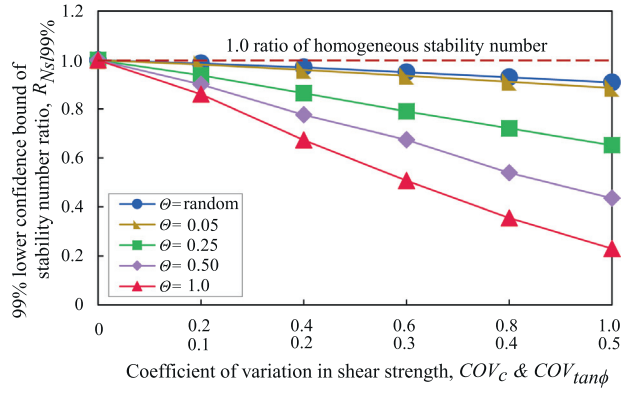


Fig. 7. 99 % lower confidence bound of stability number ratio.

ually increases. Based on this recovery tendency, Zhu et al. (2019) introduced a worst-case correlation length, considering the appearance of the highest probability of failure. In fact, it should be noted that the normalized correlation length used in prior studies, by Kasama and Whittle (2015) and Zhu et al. (2019), ranges from 0 to 4.0 and 0 to 100.0, respectively. Compared to the above-mentioned prior studies, the range in normalized correlation length in our study (0 to 1.0) is thought to be small. That is the main reason for the decrease in the stability number in the present study. On the other hand, the range in $COV_s$ is another important reason. Based on the results for the probability of slope failure for a wide range of $COV_s$ (0 to 10.0), by Griffiths and Fenton (2004), there are threshold values for $COV_s$ that can determine the increasing and decreasing trends of the probability of failure (the threshold $COV_s = 1.0783$ by the single random variable approach (*SRV*) and the threshold $COV_s = 0.65$ by the *RFEM*). Comparing our numerical results for $COV_s = 0$–1.0 with their findings, it is thought that the decrease in the stability number with the increasing correlation length results in an increase in the probability of failure.

Fig. 8 demonstrates the mean stability number ratio $\mu_{R_{Ns}}$ against the slope angle, considering spatial variability. The upper curves represent small $COV_s$ and are almost horizontal, suggesting that the reduction in $\mu_{R_{Ns}}$ by spatial variability is somewhat similar for each slope angle. However, as $COV_s$ increases, the difference in the reduction in $\mu_{R_{Ns}}$ between each slope angle becomes increasingly significant. The maximum reduction in $\mu_{R_{Ns}}$ is at a slope of $\beta = 60°$, while the minimum is at a slope of $\beta = 30°$. Such differing effects of spatial variability on flat and steep slopes will be investigated later.

Fig. 9 illustrates the effect of spatial variability on the mean stability number ratio with respect to the cross-correlation coefficient between shear strength components $c$ and $\tan\phi$. It is seen that generally the stability number decreases with increases in $COV_s$ and $\Theta$, regardless of the positive or negative cross-correlation coefficient. However, it should be noted that, for the same $COV_s$ and $\Theta$, the stability number for a positive cross-correlation coefficient is smaller than that for a negative one, and that the results for the zero cross-correlation coefficient lie between them. Therefore, positive and negative $\rho$ have a similar effect on the reduction in the stability number, and the results obtained when using a positive $\rho$ lie on the safer side (Griffiths et al. 2009; Javankhoshdel and Bathurst 2016; Zhang et al. 2021).

### 3.2. Sliding volume evaluation

The stability number (factor of safety) method of performing slope stability evaluations is apparent and effective. However, evaluations based only on the safety factor are not fully informative. Fortunately, one benefit of a 3D slope analysis is that the output information on the volume of a sliding mass provides other insights into a slope stability assessment. Furthermore, a 3D analysis with various sliding volumes also provides a deeper understanding of the effect of spatial variability on slope stability. In order to evaluate the slope failure dimension, this paper considers a sliding volume $V$ as an investigated parameter, including mean average sliding volume $\mu_V$ and its standard deviation $\sigma_V$.

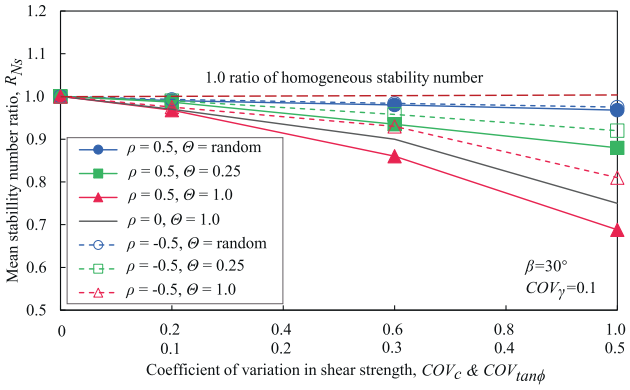


Fig. 9. Influence of cross-correlation coefficient $\rho$ on mean stability number ratio considering spatial variability.

$$\mu_V = \frac{1}{n}\sum_{1}^{n} V_i \quad \sigma_V = \sqrt{\frac{1}{n-1}\sum_{1}^{n}(V_i - \mu_V)^2} \tag{14}$$

where $V_i$ is the sliding volume for the $i$th iteration, and $\mu_V$ and $\sigma_V$ are the mean and standard deviations of the sliding volume for each complete iteration of *MCS*.

Fig. 10 (a) shows the cumulative mean sliding volume against the number of *MCS* iterations. It shows that 1000 iterations are sufficient to acquire accurate results for a given *COV* of shear strength. Fig. 10 (b) shows the cumulative *COV* of the sliding volume against the number of *MCS* iterations. It is clear that the variable sliding volume becomes stable within 1000 iterations. Hence, incorporating the observations from Fig. 3, it is suggested that a set of 1000 iterations of *MCS* is adequate to obtain a reliable statistical interpretation. As pointed out by Xiao et al. (2016), a more accurate estimation could be acquired from a larger number of *MCS*, but computational costs must be taken into consideration.

Histograms of the sliding volumes for $\beta = 30°$, $COV_\gamma = 0.1$, and $COV_s = 1.0$ and 0.5 from one complete series of *MCS* are presented in Fig. 11. In general, all distributions of sliding volumes lead to less than homogeneous slope results, and all shapes of distributions are changed by increasing the spatial variability, suggesting that the sliding volume is significantly affected by the spatial variability. In other words, for a relatively small $\Theta$ ($\Theta = 0.25$; see Fig. 11 (a)), the results of $V$ can be fitted as a normal distribution. However, the applicability of the normal distribution lessens with an increasing $COV_s$, suggesting that the fit quality for a large $COV_s$ is worse than that for a small $COV_s$. For a relatively large $\Theta$ ($\Theta$ = 1.0; see Fig. 11 (b)), the normal distribution cannot be fitted. The detailed results shown in Table 2 were estimated by *K-S* normality tests. As a result, a log-normal distribution is considered for $\Theta$ = 1.0 in Fig. 11 (b). However, at the large $COV_s$ values of 1.0 and 0.5, the log-normal distribution no longer fits. The histogram does not follow the log-normal distribution curve, shown by the bold italic values in the *K-S* normality test results given in Table 2.

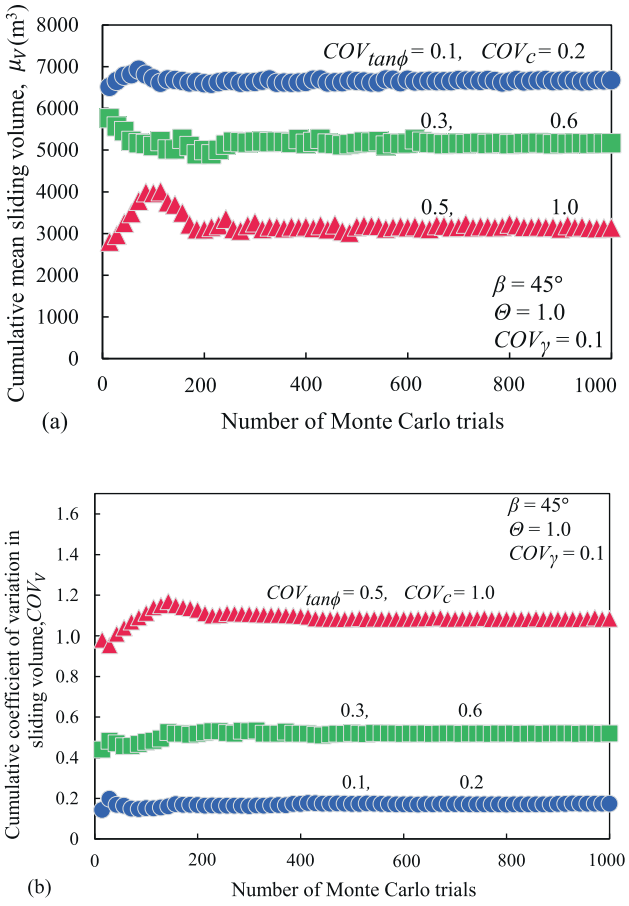


Fig. 10. Cumulative mean and *COV* of sliding volume in Monte Carlo trials: (a) cumulative mean sliding volume and (b) cumulative *COV* of sliding volume.

Fig. 12 depicts the relationships between mean sliding volume $\mu_V$ for $\Theta = 1.0$ and the slope angle. The red dashed line is the resulting sliding volume for a homogeneous slope, $V_{hom}$. It is seen that $V_{hom}$ decreases with an increasing slope angle, with apparently small values for $\beta = 45°$ and 60° compared with $\beta = 30°$. The effect of the decreasing sliding volume with the increasing slope angle can still be observed in the spatial variable slope, and the maximum and minimum values of the mean sliding volume can be found at $\beta = 30°$ and 60°, respectively. Considering the $COV_s$ influence, $\mu_V$ decreases for all slope angles with an increasing $COV_s$. However, for small $COV_s$ ($COV_c$ and $COV_{tan\phi}$ = 0.2 and 0.1) at $\beta = 45°$, the $\mu_V$ of a spatially variable slope is larger than that of a homogeneous slope. This notable observation will be further discussed.

Fig. 13 plots the *COV* of sliding volume $COV_V$, considering spatial variability. It shows that $COV_V$ increases with increasing $COV_s$, and that the increasing rate of $COV_V$ also increases with $\Theta$. A comparison between $COV_{N_s}$ in Fig. 6 and $COV_V$ in Fig. 13 clarifies that the variation in the stability number is less than that of the sliding volume (0.27 maximum $COV_{Ns}$ < 1.18 maximum $COV_V$). This suggests that the slope failure dimension of such a sliding volume is largely affected by the spatial variability. This

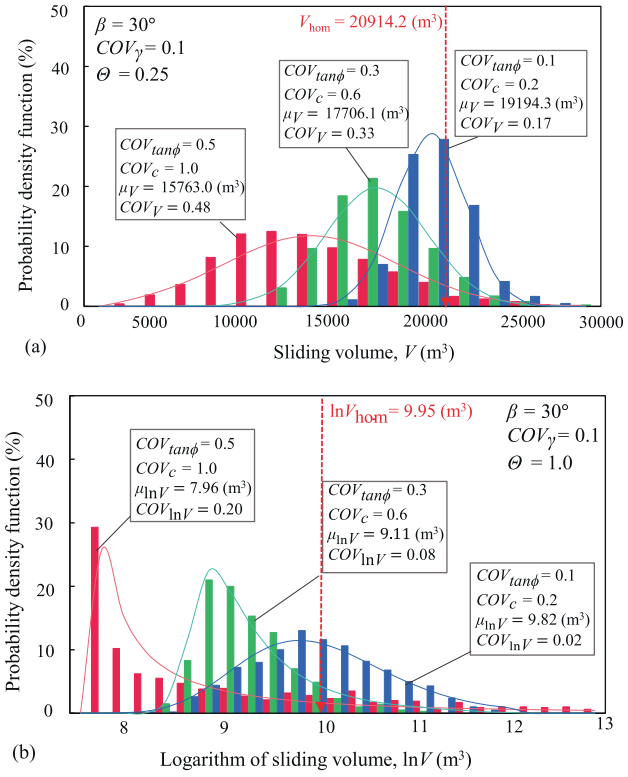


Fig. 11. Probability density function of sliding volume: (a) normal distribution and (b) log-normal distribution.

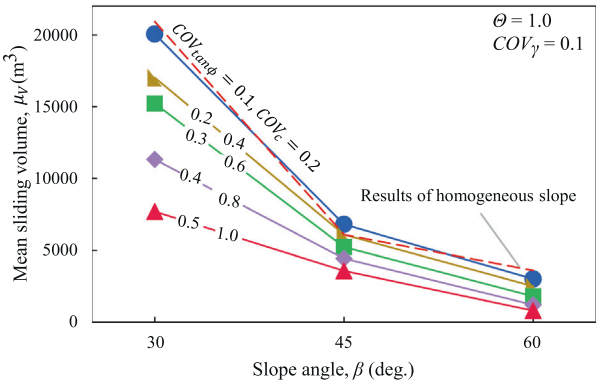


Fig. 12. Mean sliding volume against slope angle.

large variation in sliding volume at large $COV_s$ values will be investigated. It is firstly doubted here, due to the existence of different failure mechanisms.

Similar to the stability number ratio, in order to examine the sliding volume changes due to spatial variability, the sliding volume ratio $R_{vi}$ and its mean are introduced as follows:

$$R_{Vi} = \frac{V_i}{V_{\text{hom}}} \quad \mu_{R_V} = \frac{1}{n}\sum_{1}^{n} R_{V_i} \tag{15}$$

where $V_{\text{hom}}$ is the sliding volume for a homogeneous slope, $R_{vi}$ is the sliding volume ratio for each $i$th realization, and

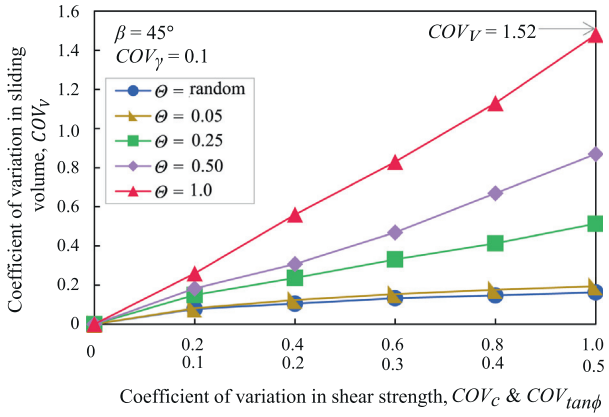


Fig. 13. Influence of spatial variability of shear strength on $COV$ of sliding volume.

$\mu_{R_V}$ is the mean of the sliding volume ratio for each complete series of $MCS$.

In reality, for sliding volume evaluations, it is not necessary to consider the sliding mass for very small volumes, especially for a small volume together with a large stability number (factor of safety). Conversely, close attention should be paid to any extremely large sliding volumes, which always lead to serious consequences. For such consideration, an evaluation of the mean sliding volume ratio and 99 % upper confidence bound of the sliding volume are presented in Fig. 14. It should be noted that the method of presenting the 99 % upper confidence bound of the sliding volume ratio in this figure differs from that in Fig. 7, which is selected from the original output data on the sliding volume at the 99 % upper bound. It is seen that $R_{V_{u99\%}}$ increases with $COV_s$ and $\Theta$, which suggests that, although increasing spatial variability results in a decreasing mean sliding volume (for instance, as shown in Fig. 12), unexpectedly large sliding volumes are prone to occur. This useful information may alert slope designers to be vigilant in terms of potential large-scale failures, even when the ground soil presents high spatial variability.

The sliding volume decreases with an increasing slope angle, and this slope angle effect is shown in Fig. 12. However, in order to evaluate the spatial variability effect on the

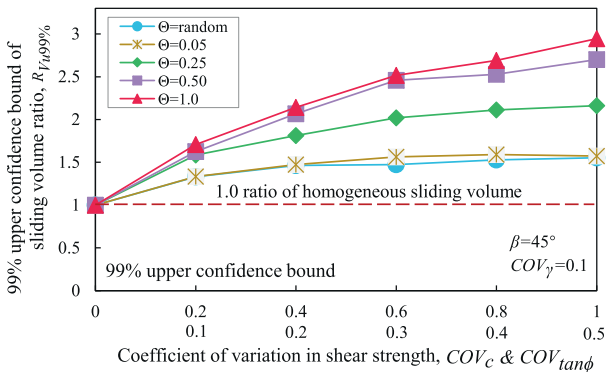


Fig. 14. 99% upper confidence bound of sliding volume ratio.

sliding volume for all slope angles, irrespective of the angle effect, the mean sliding volume ratio $\mu_{R_V}$ against the slope angle is plotted in Fig. 15. It illustrates the important point that the reduction in mean sliding volume caused by spatial variability is at its most serious at the slope angle of 30° (an 0.65 reduction when $COV_s$ is varied from 0.2 to 1.0). Another interesting point is that the mean sliding volume for a spatial variable slope is smaller than the sliding volume for a homogeneous slope, $V_{\text{hom}}$, except for the 45° slope, where the mean sliding volume for a spatially variable slope is larger than $V_{\text{hom}}$, noted as $\mu_{R_V}$ greater than 1.0 for $COV_s = 0.2$ and 0.1. This unusual finding will be investigated later. Next, the minimum reduction in $\mu_{R_V}$ is found for the 60° slope, suggesting that the spatial variability effect is not as significant as it is for the other two slope angles. In order to compare the effects of spatial variability on the stability number and sliding volume, Fig. 8 is recalled. It is seen that the reduction in $\mu_{R_V}$ is larger than that in $\mu_{R_{Ns}}$ for slope angles of 30° and 45°, and equivalent for the slope angle of 60°. Therefore, the marked effect of spatial variability on the sliding volume is seen for a shallow slope.

### 3.3. Relationship between stability number and sliding volume in terms of failure mode

In the above discussions, certain facts have been presented. For example, Fig. 8 reveals that the marked effect of spatial variability is seen for a large slope angle. Fig. 13 shows a large variation in sliding volumes triggered by large $COV_s$. Fig. 15 demonstrates a $\mu_{R_V}$ larger than 1.0 at $COV_s = 0.2$ and 0.1 for $\beta = 45°$ and a serious reduction in $\mu_{R_V}$ by spatial variability for $\beta = 30°$. These interesting and unfamiliar facts can hardly be properly understood if their interpretation is based only on the stability number and sliding volume. These are imperfect measures for quantifying slope stability since identical slopes with the same stability number and sliding volume can exhibit different failure mechanisms due to the variability of the soil properties. Therefore, an evaluation of the influence of soil spatial variability on failure mechanisms is suggested. In order to investigate the failure mechanism in the relationship between the stability number and the sliding volume, this subsection provides stability evaluations that consider the slope failure mode. As expected, two base failure modes, two face failure modes, and one toe failure mode are identified in terms of the location of the critical slip surface. As the inset drawings in the following figures show, base failure mode 1, $M_{b1}$, is characterized as a large slope failure, which includes the slope crest and slope toe in addition to the inclined slope face. The sliding mass for base failure mode 2, $M_{b2}$, includes the slope toe and inclined slope face, while that for face failure mode 1, $M_{f1}$, includes the inclined slope face and slope crest. For face failure mode 2, $M_{f2}$, the sliding mass includes only the inclined slope face. In addition to toe failure mode $M_t$, whose sliding mass includes the slope crest and the critical slip surface passing across the slope toe, there is a transition failure mode between $M_{b1}$ and $M_{f1}$. $M_{b1}$ is expressed as a large failure, while $M_{b2}$, $M_{f1}$, and $M_{f2}$ are expressed as relatively small failures. However, due to the stationary stability analysis and the inherent assumption of *LEM* methodology, it should be noted that the failure mode evaluation in this study does not account for secondary or progressive failure.

Figs. 16, 17, and 18 illustrate the relationships between stability number ratio $R_{N_s}$ and sliding volume ratio $R_V$, in terms of the failure mode, for the largest spatial variability considered in this study ($COV_s = 1.0$ and $\Theta = 1.0$). In general, a positive correlation between the stability number and the sliding volume can be found for all slope angles. It is noted that $M_{b1}$ is the deterministic failure mode for homogeneous slopes of $\beta = 30°$ and 45°, and $M_{f1}$ is the deterministic failure mode for $\beta = 60°$, suggesting that, with an increasing slope angle, the dimension of the deterministic failure change from large to small, and explaining how the sliding volume decreases as the slope angle increases. The black plots in the three figures show the locations of the means of $R_{N_s}$ and $R_V$ for each failure mode. An effect of the slope angle on the stability number can be

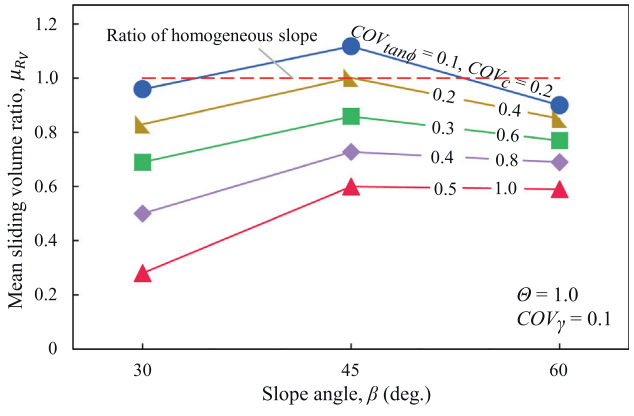


Fig. 15. Mean sliding volume ratio against slope angle.

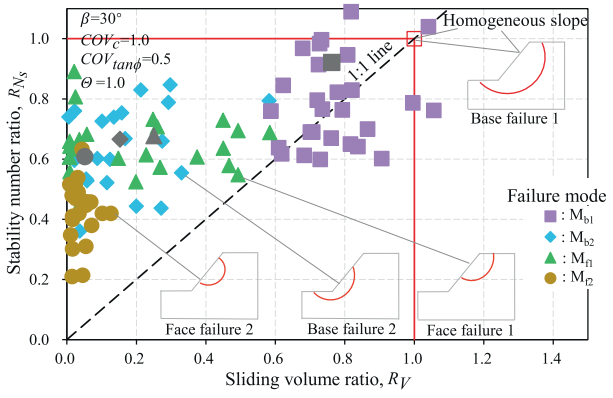


Fig. 16. Stability number ratio against sliding volume ratio with respect to failure mechanism for $\beta = 30°$.

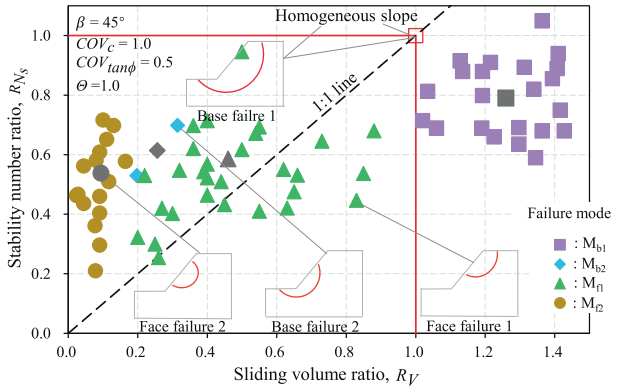


Fig. 17. Stability number ratio against sliding volume ratio with respect to failure mechanism for $\beta = 45°$.

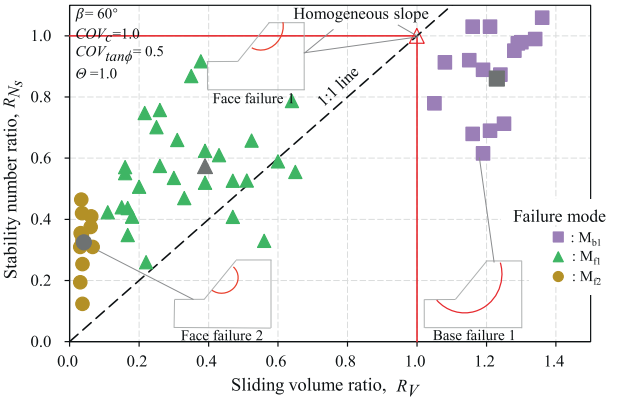


Fig. 18. Stability number ratio against sliding volume ratio with respect to failure mechanism for $\beta = 60°$.

found, whereby the stability number decreases with increases in the slope angle, even when considering the same failure mode. As expected, a large change in the sliding volume ratio via the change in failure mode is observed, which explains that the large variation in sliding volumes presented in Fig. 13 is due to the existence of various failure modes.

In Fig. 16, for the slope angle of $\beta = 30°$, the results for base failure mode $M_{b1}$ are plotted close to the 1:1 line, accompanied by large values of $R_{N_s}$ and $R_V$. The results for the other three modes ($M_{b2}$, $M_{f1}$, and $M_{f2}$) are all plotted above the 1:1 line. This means that $R_{N_s}$ is larger than $R_V$ for these three failure modes, suggesting that $RV$ is affected greatly by the failure mode. In the case of $M_{f2}$, it is noted that the range in $R_{N_s}$ is apparently larger than the range in $R_V$, which means that very different stability numbers could arise even for comparable sliding volumes. This effect further confirms that the stability of a slope is mainly controlled by the average strength along the slip surface; $M_{f2}$ is local and small enough to show the obvious spatial average effect. Fig. 18 shows that, with a slope angle of $\beta = 60°$, the $R_V$ for $M_{f1}$ in a spatially variable slope is smaller than 1.0, affirming that spatial variability leads to a reduced sliding volume when compared with that for a homogeneous slope. (The failure mode for a 60° homogeneous slope is $M_{f1}$.) Moreover, the $R_V$ for $M_{b1}$ is larger than 1.0, which confirms the large failure feature for $M_{b1}$. Finally, in Fig. 17, for a slope angle of $\beta = 45°$, the failure mode for a homogeneous slope is $M_{b1}$. However, the $R_V$ of $M_{b1}$ for a spatially variable slope is generally larger than 1.0. Thus, the sliding volume of $M_{b1}$ for a spatially variable slope is larger than that for a homogeneous slope, which is contrary to the finding that spatial variability results in a reduction in sliding volume. Hence, further assessment is required of $M_{b1}$ for homogeneous and spatially variable slopes of $\beta = 45°$.

In order to examine the effect of spatial variability on the failure mode, Figs. 19, 20, and 21 show the occurrence of each failure mode against the $COV$ of shear strength and the failure mode transition for a homogeneous slope. It is necessary to mention that the toe area of the slope should be closely monitored as the shear stress concentrates and the critical slip surface shifts from passing below the toe (base failure) to passing through the inclined face (face failure) when the slope angle increases (Stianson et al., 2011; Al-Karni and Al-Shamrani, 2000). Before introducing toe failure mode $M_t$, the failure mode for a homogeneous slope

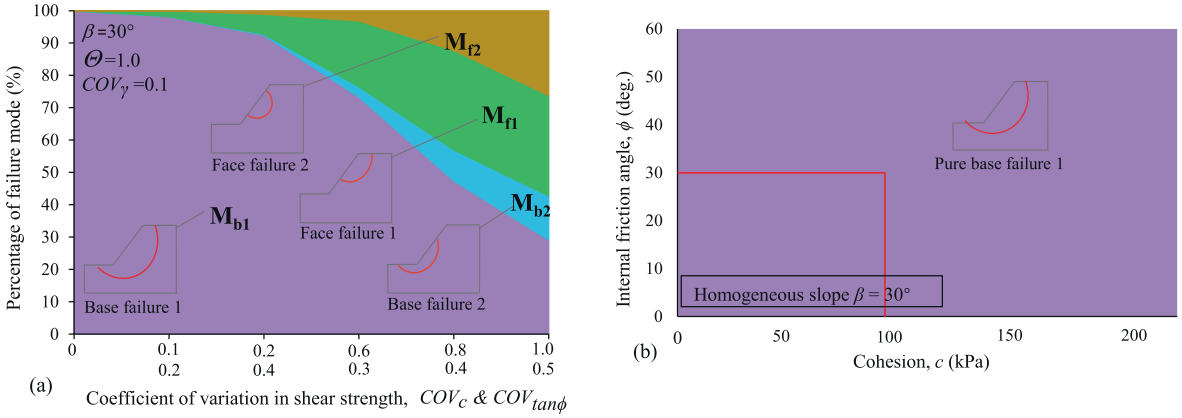


Fig. 19. Investigation of failure mode for $\beta = 30°$: (a) percentage of failure mode against $COV$ of shear strength for spatially variable slope and (b) deterministic failure mode for homogeneous slope.

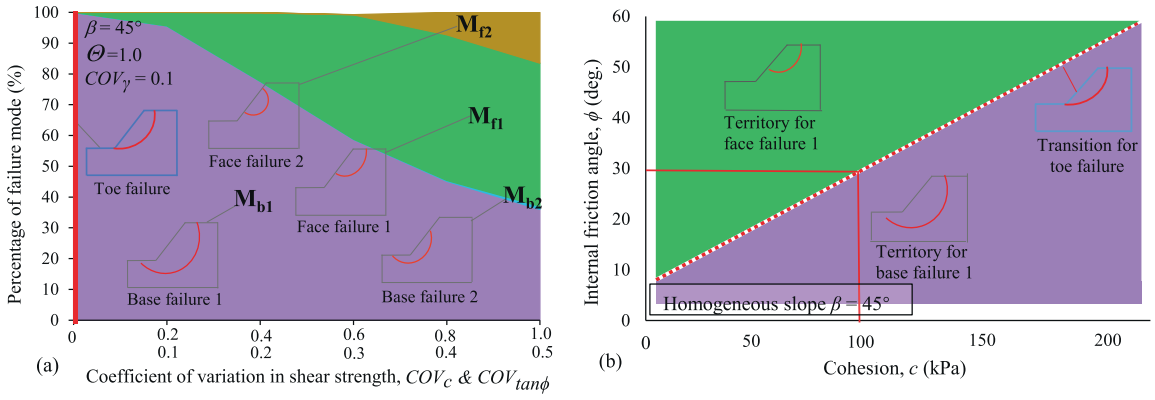


Fig. 20. Investigation of failure mode for $\beta = 45°$: (a) percentage of failure mode against $COV$ of shear strength for spatially variable slope and (b) deterministic failure mode for homogeneous slope.

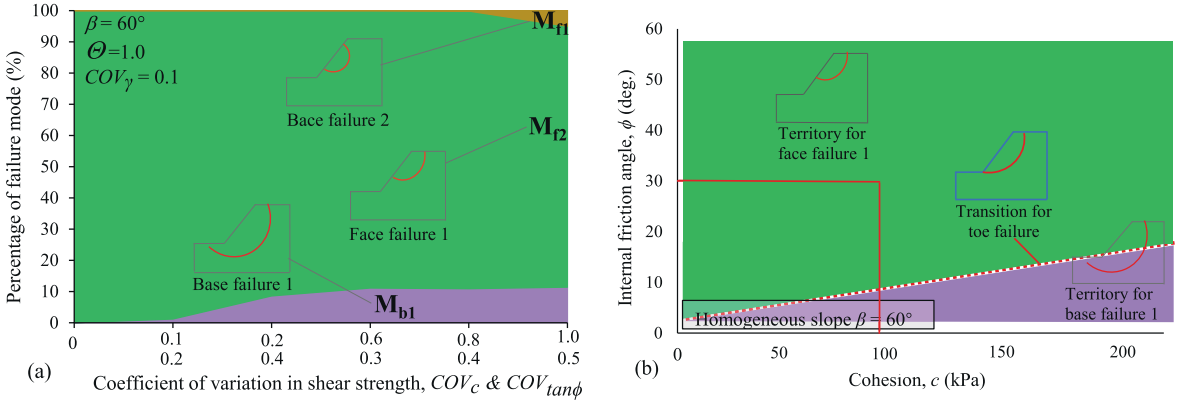


Fig. 21. Investigation of failure mode for $\beta = 60°$: (a) percentage of failure mode against $COV$ of shear strength for spatially variable slope and (b) deterministic failure mode for homogeneous slope.

of $\beta = 45°$ is firstly characterized as $M_{b1}$ ($M^{45^\circ}_{hom} = M_{b1}$). As found in Fig. 17, the $\mu_{R_Y}$ of $M_{b1}$ for a spatially variable slope is larger than 1.0, which means that the sliding volume of $M_{b1}$ for a spatially variable slope is larger than that of $M_{b1}$ for a homogeneous slope ($V^{45^\circ}_{SV(M_{b1})} > V^{45^\circ}_{hom(M_{b1})}$). This suggests that the critical slip surface of $M_{b1}$, for a spatially variable slope, sits deeper and passes below the toe. Conversely, the critical slip surface for a homogeneous slope should be close to the toe and pass across it. Under these mechanisms, toe failure mode $M_t$ is introduced; it lies between base failure $M_{b1}$ and face failure $M_{f1}$. It is featured as the critical failure surface passing across the slope toe and is sketched in the following figures. In order to investigate the mechanism of transition mode $M_t$, Fig. 19 (b), 20 (b), and 21 (b) show the failure mode transitions for the homogeneous shear strength of slope angles $\beta = 30°$, 45°, and 60°, respectively. It is seen that, under homogeneous shear strength, pure base failure mode $M_{b1}$ for $\beta = 30°$, failure modes $M_{b1}$ and $M_{f1}$, and toe mode $M_t$ are observed for $\beta = 45°$ and 60°. This clearly suggests that $M_{b1}$, $M_{f1}$, and $M_t$ are the deterministic failure modes for a homogeneous slope and that $M_{b2}$ and $M_{f2}$ are the results of spatial variability. It can also be seen that homogeneous slope failures all involve the slope crest ($M_{b1}$, $M_t$, and $M_{f1}$). In addition to the range in $c$–$\phi$ values of those failure modes for slopes of $\beta = 45°$ and 60° in Fig. 20 (b) and 21 (b), it is seen that plots for $M_{b1}$ lie in the lower portion, indicating a combination of large cohesion $c$ and small friction angle $\phi$, contrasting the combination of small $c$ and large $\phi$ for $M_{f1}$. This observation agrees with the study of Chen and Chameau (1983), who evaluated a 3D $c$–$\phi$ slope and found that lower $c$ values with higher $\phi$ values lead to a shallow critical sliding surface passing over the toe, while higher $c$ values with lower $\phi$ values lead to a deep critical sliding surface extending beyond the toe of the slope (referred to as $M_{f1}$ and $M_{b1}$, respectively, in this study). Hence, the sliding volume sequence of $V_{M_{b1}} \geq V_{M_t} \geq V_{M_{f1}}$ is provided. Since the changes in $M_{b1}$ and $M_{f1}$ are due to changes in the values of $c$ and $\phi$, a series of deterministic values of $c$ and $\phi$ for $M_t$, which may be called $c$–$\phi$ thresholds for $M_{b1}$ and $M_{f1}$ transitions, are discovered and then plotted as red dashed lines in the figures. The values $c = 100$ kPa and $\phi = 30°$, shown as red solid lines, are the mean strengths used as inputs in this study. They are exactly the threshold values causing toe failure

$M_t$ for a slope of $\beta = 45°$. This further indicates that a normalization index for a sliding volume ratio, that considers the sliding volume for a homogeneous slope of $\beta = 45°$ ($V_{Mt}$), will result in a ratio larger than 1.0 at a small $COV_s$ ($COV_s = 0.2$ and 0.1) since the large base failure $M_{b1}$ is also dominant at that $COV_s$. It consequently explains how $\mu_{R_V}$ lies above the 1.0 ratio line for a small $COV_s$ (0.2), as shown in Fig. 15, and why, when the $COV_s$ increases, as shown in Fig. 20, the $M_{b1}$ is gradually replaced by other small failure modes and $\mu_{R_V}$ eventually drops below 1.0.

At $\beta = 60°$, as shown in Fig. 21 (a), the failure mode for a homogeneous slope is face failure $M_{f1}$ ($M_{hom}^{60^\circ} = M_{f1}$). $M_{f1}$ is the dominant failure mode irrespective of any changes in $COV_s$. This suggests that spatial variability has less influence on the failure mechanism of a steep slope. The common occurrence of $M_{f1}$ indicates a low variation in the failure mode, and further explains it having the smallest change in sliding volume ratio among all the slope angles, as shown in Fig. 15. In Fig. 19 (a), for a homogenous shallow slope ($\beta = 30°$), the failure mode is $M_{f1}$ ($M_{hom}^{30^\circ} = M_{f1}$). It is seen that $COV_s$ has a significant influence on the failure mode. For small $COV_s$ of 0.2 to 0.4, $M_{b1}$ is dominant, with a probability of more than 90 %. However, as $COV_s$ increases, the failure mode gradually changes to the modes for small failures. Eventually, all kinds of failure modes appear. And, at $COV_s = 1.0$, more than 70 % of the occurrences are small failure modes ($M_{b2}$, $M_{f1}$, and $M_{f2}$). For the sliding volume ratio, therefore, a normalized index considers the sliding volume of a homogeneous slope ($V_{M_{b1}}$), resulting in a small sliding volume ratio $R_V$ together with an increased occurrence of small failure modes at large $COV_s$ values. The results of the maximum reduction in the sliding volume ratio are shown in Fig. 15. It can be concluded that the sliding volume evaluation for a shallow slope is conservative, regardless of the soil's spatial variability.

In order to evaluate the failure mechanism together with the slope inclination, Fig. 22 presents the percentages of failure modes against the slope angle for $COV_s = 0.5$ and 1.0 and $\Theta = 1.0$. It is found that $M_{f1}$ becomes the major failure mode, while $M_{b2}$ gradually fades away as the slope angle steepens, and disappears at $\beta = 60°$. It is noted that $M_{b1}$ and $M_{f1}$, whose sliding masses include the slope crest, become the major failure modes as the slope angle increases, with a combined 94 % probability at $\beta = 60°$. This shows that failures involving the slope crest comprise the main failure mechanism for steep slopes, while failures involving the toe ($M_{b1}$ and $M_{b2}$) gradually become minor. It is also found that, as the slope angle decreases, the slope failure mechanism varies greatly. For example, four failure modes can be found at $\beta = 30°$ and their probabilities of occurrence are relatively comparable.

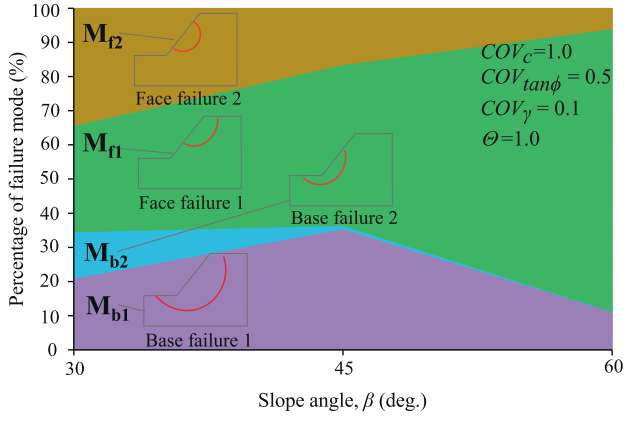


Fig. 22. Percentage of failure mode against slope angle for spatially variable slope.

### 3.4. Sensitivity analysis

Sensitivity analyses are often carried out to determine the relationship between the uncertainty in the output of a model and the different sources of uncertainty in its input. Zhang et al. (2017) conducted a sensitivity analysis between various parameters and the corresponding factor of safety for the Sweden arc method, using a first-order derivation method. El-Ramly et al. (2002) performed a probabilistic sensitivity analysis to quantify the contributions of the various sources of uncertainty in geotechnical parameters to the overall design uncertainty. Khan and Malik (2013), Chen et al. (2016), Chen et al. (2019), and Kasama et al. (2021a) investigated the effect of geotechnical parameters on structures by sensitivity analyses. In this study, the geotechnical parameters for slope stability are cohesion $c$, friction angle $\phi$ ($\tan\phi$), and unit weight $\gamma$, which are also treated as random variables for modeling the soil uncertainty. (Table 1 summarizes the mean averages and variances for all parameters.) It is necessary to evaluate the sensitivity of those parameters, and the stability number of this slope stability model.

In order to evaluate the sensitivity of input random parameters, whose uncertainties are deemed important to slope stability, El-Ramly et al. (2002) performed a sensitivity analysis with Spearman rank correlation coefficients as input. The Spearman rank correlation coefficient is a commonly used nonparametric measure of rank correlation that reveals the strength of a relationship between two sets of associated data. It varies between –1 and 1, the former indicating a perfect negative correlation, the latter a perfect positive correlation. A zero value indicates no correlation between the two data sets. This technique can be employed to measure the correlation between and the contribution of each input variable to the uncertainty in the stability number in this study (Conover, 1999). In order to measure the correlation between two random variables under the condition whereby the indirect influence of other random variables is eliminated, a partial estimation is introduced as a partial Spearman rank correlation coefficient (Conover, 1999). The formulas to calculate the first order and second order partial Spearman rank correlation coefficients are introduced as follows:

$$\rho_{(XW;Y)} = \frac{\rho_{XW} - \rho_{XY}\rho_{YW}}{\sqrt{(1-\rho_{XY}^2)(1-\rho_{YW}^2)}} \tag{16}$$

where $\rho_{AB}$ is the Spearman rank correlation coefficient between $A$ and $B$, and $\rho_{(AB,C)}$ is the first order partial Spearman rank correlation coefficient between $A$ and $B$ after controlling the effect of $C$.

$$\rho_{(XW;Y,Z)} = \frac{\rho_{XW;Y} - \rho_{XZ;Y}\rho_{WZ;Y}}{\sqrt{(1-\rho_{XZ;Y}^2)(1-\rho_{WZ;Y}^2)}} \tag{17}$$

where $\rho_{(AB;C,D)}$ is the second-order partial Spearman rank correlation coefficient between $A$ and $B$ after controlling the effect of $C$ and $D$.

Three parameters ($c$, $\phi$, and $\gamma$) are considered in this study. Hence, Eq. (17), for the second-order partial Spearman rank correlation coefficient, is used to estimate the relationship between one input parameter and output $N_s$, after controlling the effect of the other two parameters. To perform a sensitivity analysis using a partial Spearman rank correlation coefficient, the random parameters for shear strength $c$ and $\phi$ are assumed to be the average cohesion and average friction angle along the slip surface, respectively. In addition to the above two shear strength parameters, unit weight $\gamma$ is treated as the average weight of the soil mass above the slip surface. These assumptions could reduce the uncertainty of the soil properties along the slope surface. However, it has been established that slope failure tends to occur when the average strength along the slip surface is insufficient, rather than because of weak soil strength at a particular location (Kasama and Whittle, 2015). This spatial averaging effect is also evidenced by Fig. 6. The assumption for the uncertainty of the average shear strength along the slip surface is reasonable and makes for an accurate assessment of the uncertainty.

Fig. 23 shows the sensitivity analysis using partial Spearman rank correlation coefficients for the three input variables. The inset figure with grey bars shows the partial Spearman rank correlation coefficients without considering the failure mechanism. The two shear strength parameters

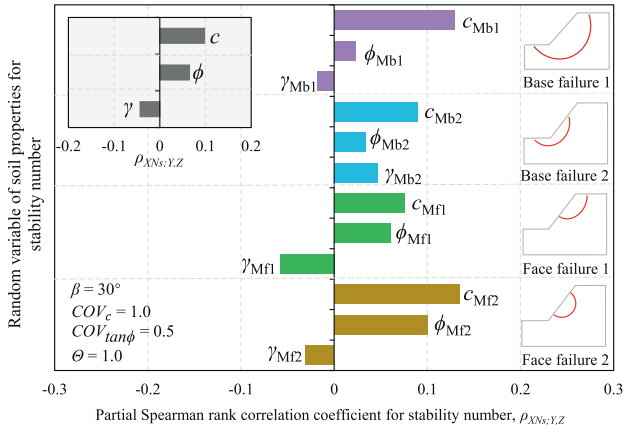


Fig. 23. Partial Spearman rank correlation coefficient for stability number with and without consideration of failure mode.

($c$ and $\phi$) are positively correlated with the stability number. This is due to the definition of the stability number (factor of safety) in terms of the shear strength and Mohr-Coulomb failure criterion. In addition to unit weight $\gamma$, a negative correlation to $N_s$ is revealed, which means that an increase in unit weight tends to decrease the stability number. This is reasonable since the unit weight mainly contributes to the slope sliding driving force. It is seen that the most sensitive input parameter is cohesion $c$. The reason for its maximum influence is that its probability density function range is larger than those of $\phi$ and $\gamma$; thus, it can produce large changes in the stability number. However, as pointed out by Zhang et al. (2017), many studies ignore the influence of the sensitivity of parameters on the slope failure mode and give an overall sensitivity evaluation, as in the inset figure, which is inaccurate if the slope behavior points to various failure mechanisms. In this study, various failure modes have been identified. In order to reveal informative details and enhance the reliability of the sensitivity analysis, failure modes considering the partial Spearman rank coefficient correlations were examined, and are shown in Fig. 23. In general, cohesion $c$ remains the most sensitive soil parameter in each failure mode, which confirms its dominant influence on the stability number in this slope stability model and the positive contributions of the two shear strength parameters. It is worth noting that a positive correlation of unit weight $\gamma$ is revealed for base failure $M_{b2}$, meaning that $\gamma$ also contributes to slope stability. This apparently odd finding is in fact reasonable, if the sliding mass is mainly located at the slope base, as it could stop the above sliding mass and provide a moment counter to the sliding moment. Hence, a positive correlation of $\gamma$ is found for $M_{b2}$. The magnitude of the negative correlation of $\gamma$ for $M_{b1}$ is smaller than that for face failures $M_{f1}$ and $M_{f2}$, for the same reason, since the positive effect of $\gamma$ has been offset by a large volume of upper sliding mass. Meanwhile, the largest negative correlation of $\gamma$ is found for $M_{f1}$, a face failure involving the slope crest. In addition to the engineering interest of the largest failure, $M_{b1}$, cohesion has the largest positive correlation to slope stability, while the unit weight has an insignificant negative influence. These results highlight the necessity of considering the failure mechanism in any sensitivity analysis, as it could affect the judgment of uncertainty in slope stability.

### 3.5. Significance of mean values of shear strength parameters

Depending on the material type, a large mean cohesion with a small mean friction angle for clayey soil, a small mean cohesion with a large mean friction angle for sandy soil, and relatively large cohesion and a relatively large friction angle are usually seen for soil-rock mixtures. The current analyses were made using relatively large mean values for cohesion $\mu_c = 100$ kPa and for the friction angle of $\mu_\phi = 30°$ and are referred to as the shear strength parameters for soil-rock mixtures. In order to consider the effect of different types of soil and other possible combinations of

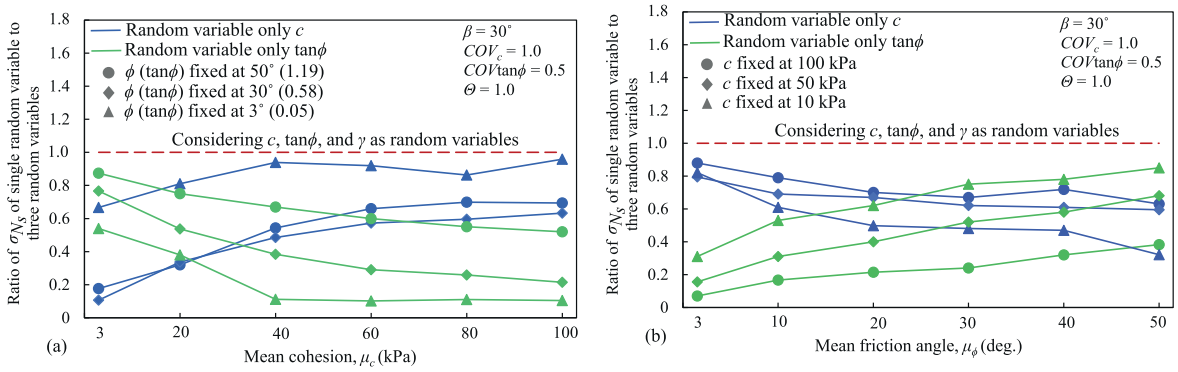


Fig. 24. Ratio of $\sigma_{N_s}$ for single random variable to all three random variables: (a) considering different mean cohesion values and (b) considering different mean friction angles.

mean values for the shear strength parameters on the analysis results, additional calculations were performed.

Fig. 24 demonstrates the significance of random variables for the shear strength parameters (cohesion $c$ and friction angle $\phi$) considering their different mean values. When investigating the single random variable, the others are kept constant at their means, and a ratio of the variation in $N_s$ resulting from a single random variable to that resulting from the simultaneous input of all three random variables is introduced in Eq. (18), and the results are plotted in Fig. 24. It should be noted that the effect of the random variables on the soil unit weight is not shown in the figure, due to the fixed mean value of 20 kN/m$^3$ used in the analyses.

$$R = \sigma_{N_s\_\text{single}} / \sigma_{N_s\_\text{three}} \tag{18}$$

Fig. 24 (a) and (b) show mean cohesion $\mu_c$ changing from 3 kPa to 100 kPa, while keeping the mean friction angles of $\mu_\phi = 3°$, 30°, and 50°, and mean friction angle $\mu_\phi$ changing from 3° to 50°, while keeping the mean cohesion values of $\mu_c = 10$ kPa, 50 kPa, and 100 kPa, respectively, while the mean unit weight is fixed as $\mu_\gamma = 20$ kN/m$^3$. Each random variable has a different magnitude of significance in the output of the model (referred to as a variation in $N_s$).

Considering sandy soil with small cohesion and a large friction angle, for example, $\mu_c = 3$ kPa with $\mu_\phi = 30°$ and 50°, as in Fig. 23 (a), the variation in $N_s$ for the cases where only the friction angle is considered as a random variable is the most significant. This means that the variation in friction angle is the major source of the variation in $N_s$ at the sandy soil condition of $\mu_c = 3$ kPa with $\mu_\phi = 30°$ and 50°. When considering other possible combinations and increasing the mean cohesion (3 kPa to 100 kPa), the significance of the friction angle decreases, while the significance of cohesion increases and surpasses that of the friction angle. On the other hand, considering clayey soil with a small friction angle and large cohesion, for instance, $\mu_\phi = 3°$ with $\mu_c = 10$ kPa, 50 kPa, and 100 kPa, as in Fig. 23 (b), the cohesion is the major source of the variation in $N_s$. When considering other possible combinations and increasing the mean friction angle (3° to 50°), the significance of cohesion decreases and the significance of the friction angle increases and surpasses that of cohesion, when keeping $\mu_c = 10$ kPa and 50 kPa, but it does not surpass that of cohesion when keeping $\mu_c = 100$ kPa, which is mainly due to a relatively large mean value for cohesion. Hence, a significant effect of cohesion is found in soil-rock mixtures with $\mu_c = 100$ kPa and $\mu_\phi = 30°$, such as that mainly investigated in this study.

## 4. Conclusions

This paper presented the results of a probabilistic slope stability analysis, considering the 3D spatial variation in soil properties, using a random limit equilibrium method and Monte Carlo simulation. The main conclusions are as follows.

(1) One thousand iterations of the Monte Carlo simulation (*MCS*) meet the accuracy requirement in this study, considering the cumulative mean and coefficient of variation (*COV*) of the stability number ratio and sliding volume ratio. A normal or log-normal distribution is highly adaptable to statistical distributions of the stability number and sliding volume. An assessment of the Kolmogorov–Smirnov goodness of fit test, with an acceptance criterion of $D_{n,\alpha}[1000, 0.01] = 1.035$, accounts for the uncertainty effect on the slope stability number and sliding volume and facilitates a probabilistic assessment of slope stability.

(2) The ratio of the stability number normalized by that for a homogeneous slope is <1.0 and decreases with the increasing *COV* of the shear strength and correlation length $\Theta$. The maximum decrease in the mean stability number ratio, considering the 99 % lower confidence bound, is 14 %. This occurs when $\Theta$ varies from 0.05 to 0.25 for a given $COV_s$ ($COV_c$ and $COV_{\tan\phi}$) = 1.0 and 0.5. The marked reduction in the stability number ratio is seen for steep slope angles.

(3) The ratio of the stochastic sliding volume normalized by that for a homogeneous slope decreases with increasing $\Theta$, while the 99 % upper bound of the sliding volume ratio shows a maximum decrease of 29 % when $\Theta$ varies from 0.25 to 0.50 for a given $COV_s = 1.0$ and 0.5. This marked reduction in the sliding volume ratio is seen for shallow

slope angles. The sliding volume is more sensitive to the spatial variability of the soil strength, compared to the stability number.

(4) The variations in the stability number and sliding volume are found to increase with increasing $COV_s$ and $\Theta$, due to the varied failure mechanisms at large values of $COV_s$ and $\Theta$. Five failure mechanisms (two base failures, two face failures, and one toe failure, namely, $M_{b1}$ and $M_{b2}$, $M_{f1}$ and $M_{f2}$, and $M_t$) are identified by the location of the slip surface of the sliding soil mass. The deterministic failure modes are $M_{b1}$ for a homogeneous slope of $\beta = 30°$, $M_t$ for that of $\beta = 45°$, and $M_{f1}$ for that of $\beta = 60°$. This indicates that $M_{b2}$ and $M_{f2}$ are additional failure modes triggered by soil spatial variability. Meanwhile, the failure mode varies for shallow slopes, while failure involving the slope crest is the main mechanism for steep slopes. As the slope angle increases, the failure mechanism at the critical surface is prone to change, from passing below the toe to passing above it.

(5) The sensitivity of input random variables (cohesion, friction angle, and unit weight) to the output of the stability number is evaluated considering failure mechanisms by using partial Spearman rank correlation coefficients. A positive correlation between the unit weight and the stability number can be triggered by the base failure mechanism, suggesting that sensitivity analyses should not ignore the effect of failure mechanisms.

(6) The significance of the mean values for the shear strength parameters (cohesion $c$ and friction angle $\phi$) was investigated under the consideration of different soil types. Results show that $c$ is significant in clayey soil with a large $\mu_c$ and a small $\mu_\phi$, and that $\phi$ is significant in sandy soil with a small $\mu_c$ and a large $\mu_\phi$. Considering soil-rock mixtures with a relatively large mean value for cohesion ($\mu_c = 100$ kPa) and a friction angle of $\mu_\phi = 30°$, such as the mixture mainly investigated in this study, cohesion is the most significant random variable causing a variation in the stability number, as a larger mean value is applied for it.

## Declaration of Competing Interest

The authors declare that they have no known competing financial interests or personal relationships that could have appeared to influence the work reported in this paper.

## Acknowledgements

This research was supported by JST SPRING, Grant Number JPMJSP2106, and JSPS KAKENHI, Grant Numbers 19H00812 and 20H00266.

## Appendix A.

(See Table A1, Table A2).

Table A1
Stability number, sliding volume, and g/Goodness-of-fit results for normal and log-normal distributions of $\beta = 45°$.

| $\Theta$ | $COV_c$ & $\tan\phi$ | $\mu_{Ns}$ | $\beta = 45°$ | | | | | | | | $\mu_{\ln(V)}$ | $\sigma_{\ln(V)}$ | $D_{n,\mathrm{adj}}$ |
|---|---|---|---|---|---|---|---|---|---|---|---|---|---|
| | | | $\sigma_{Ns}$ | $D_{n,\mathrm{adj}}$ | $\mu_{\ln(Ns)}$ | $\sigma_{\ln(Ns)}$ | $D_{n,\mathrm{adj}}$ | $\mu_V$ (m$^3$) | $\sigma_V$ (m$^3$) | $D_{n,\mathrm{adj}}$ | | | |
| Random | 0.2 & 0.1 | 11.99 | 0.0267 | 0.7843 | 2.48 | 0.0022 | 0.6874 | 7006.26 | 547.99 | 0.7024 | 8.85 | 0.0772 | 0.6457 |
| | 0.4 & 0.2 | 11.84 | 0.0496 | 0.5349 | 2.47 | 0.0042 | 0.6781 | 6966.14 | 730.39 | 1.005 | 8.84 | 0.1040 | 0.8911 |
| | 0.6 & 0.3 | 11.66 | 0.0777 | 0.6788 | 2.46 | 0.0067 | 0.5480 | 6809.89 | 901.04 | 0.6224 | 8.82 | 0.1320 | 0.5318 |
| | 0.8 & 0.4 | 11.47 | 0.1011 | 0.5170 | 2.44 | 0.0088 | 0.6000 | 6663.50 | 983.36 | 0.8204 | 8.79 | 0.1473 | 0.5954 |
| | 1.0 & 0.5 | 11.27 | 0.1266 | 0.7132 | 2.42 | 0.0112 | 0.5099 | 6501.91 | 1059.42 | 0.8016 | 8.77 | 0.1622 | 0.4504 |
| 0.01 | 0.2 & 0.1 | 11.96 | 0.0391 | 0.9488 | 2.48 | 0.0033 | 0.8429 | 7024.39 | 568.52 | 1.0014 | 8.85 | 0.0809 | 0.9978 |
| | 0.4 & 0.2 | 11.77 | 0.0721 | 0.9317 | 2.47 | 0.0061 | 0.5998 | 6957.78 | 859.73 | 0.9985 | 8.84 | 0.1235 | 0.7151 |
| | 0.6 & 0.3 | 11.56 | 0.1050 | 0.8505 | 2.45 | 0.0091 | 0.7556 | 6853.02 | 1058.09 | 0.8193 | 8.82 | 0.1532 | 0.4920 |
| | 0.8 & 0.4 | 11.33 | 0.1381 | 0.7173 | 2.43 | 0.0122 | 0.9059 | 6622.57 | 1164.65 | 0.9245 | 8.78 | 0.1734 | 0.5143 |
| | 1.0 & 0.5 | 11.10 | 0.1679 | 0.9325 | 2.41 | 0.0152 | 0.8914 | 6448.98 | 1247.76 | 0.6946 | 8.75 | 0.1923 | 0.5664 |
| 0.25 | 0.2 & 0.1 | 11.73 | 0.1726 | 0.6854 | 2.46 | 0.0147 | 0.7914 | 7009.34 | 1047.97 | 0.8171 | 8.84 | 0.1455 | 0.9986 |
| | 0.4 & 0.2 | 11.25 | 0.3453 | 0.4698 | 2.42 | 0.0307 | 0.4270 | 6618.14 | 1566.61 | 0.7609 | 8.77 | 0.2314 | 0.6178 |
| | 0.6 & 0.3 | 10.73 | 0.5042 | 0.4564 | 2.37 | 0.0471 | 0.5635 | 6324.08 | 2091.11 | 0.6755 | 8.70 | 0.3357 | 0.5795 |
| | 0.8 & 0.4 | 10.18 | 0.6282 | 0.4038 | 2.32 | 0.0618 | 0.5201 | 5868.87 | 2442.26 | 0.7643 | 8.59 | 0.4651 | 0.6937 |
| | 1.0 & 0.5 | 9.61 | 0.7425 | 0.3564 | 2.26 | 0.0779 | 0.6779 | 5313.89 | 2729.88 | 0.8557 | 8.41 | 0.6847 | 0.7623 |
| 0.50 | 0.2 & 0.1 | 11.58 | 0.2952 | 0.6520 | 2.45 | 0.0256 | 0.7919 | 6938.90 | 1270.16 | 0.4220 | 8.83 | 0.1735 | 0.5335 |
| | 0.4 & 0.2 | 10.90 | 0.6547 | 0.4678 | 2.39 | 0.0602 | 0.5804 | 6471.16 | 1990.63 | 0.6236 | 8.73 | 0.3024 | 0.8870 |
| | 0.6 & 0.3 | 10.15 | 0.8585 | 0.4549 | 2.31 | 0.0855 | 0.8414 | 5835.92 | 2734.95 | 0.8608 | 8.56 | 0.4937 | 0.8739 |
| | 0.8 & 0.4 | 9.25 | 1.1744 | 0.4232 | 2.22 | 0.1296 | 0.6508 | 4837.03 | 3236.41 | ***1.2901*** | 8.20 | 0.8803 | ***1.3412*** |
| | 1.0 & 0.5 | 8.31 | 1.3039 | 0.4119 | 2.10 | 0.1598 | 0.4835 | 3769.67 | 3280.77 | ***2.1614*** | 7.73 | 1.1741 | ***2.7685*** |
| 1.0 | 0.2 & 0.1 | 11.46 | 0.4552 | 0.7283 | 2.44 | 0.0399 | 0.7921 | 6807.06 | 1176.13 | ***1.0671*** | 8.81 | 0.1625 | 0.5719 |
| | 0.4 & 0.2 | 10.67 | 1.0125 | 0.3996 | 2.35 | 0.0970 | 0.4802 | 6098.59 | 1997.00 | ***1.2690*** | 8.67 | 0.3180 | 0.8502 |
| | 0.6 & 0.3 | 9.46 | 1.4231 | 0.5262 | 2.24 | 0.1513 | 0.3157 | 5229.94 | 2787.53 | ***2.0832*** | 8.41 | 0.6012 | ***1.5926*** |
| | 0.8 & 0.4 | 8.43 | 1.7766 | 0.7371 | 2.11 | 0.2142 | 0.5079 | 4431.42 | 3495.23 | ***3.4661*** | 8.04 | 0.9710 | ***1.5854*** |
| | 1.0 & 0.5 | 7.11 | 2.7724 | 0.9514 | 1.96 | 0.2729 | 0.4088 | 3575.84 | 3890.61 | ***5.9290*** | 7.56 | 1.2491 | ***1.6272*** |

Note: Acceptance criterion $D_{n,\alpha}[1000, 0.01] \leq 1.035$.

Table A2
Stability number, sliding volume, and g/Goodness-of-fit results for normal and log-normal distributions of $\beta = 60°$.

| $\Theta$ | $COV_c$ & $_{\tan\phi}$ | $\mu_{Ns}$ | $\beta = 60°$ | | | | | | | | $\mu_{\ln(V)}$ | $\sigma_{\ln(V)}$ | $D_{n,\mathrm{adj}}$ |
|---|---|---|---|---|---|---|---|---|---|---|---|---|---|
| | | | $\sigma_{Ns}$ | $D_{n,\mathrm{adj}}$ | $\mu_{\ln(Ns)}$ | $\sigma_{\ln(Ns)}$ | $D_{n,\mathrm{adj}}$ | $\mu_V$ ($m^3$) | $\sigma_V$ ($m^3$) | $D_{n,\mathrm{adj}}$ | | | |
| Random | 0.2 & 0.1 | 9.55 | 0.0284 | 0.7606 | 2.26 | 0.0030 | 0.7620 | 4142.25 | 273.62 | 0.6784 | 8.33 | 0.0690 | 0.7715 |
| | 0.4 & 0.2 | 9.38 | 0.0560 | 0.7495 | 2.24 | 0.0060 | 0.9239 | 3927.16 | 407.39 | 0.7437 | 8.27 | 0.1065 | 0.6112 |
| | 0.6 & 0.3 | 9.18 | 0.0856 | 0.9963 | 2.22 | 0.0093 | 0.6438 | 3859.67 | 490.61 | 0.7521 | 8.25 | 0.1285 | 0.6879 |
| | 0.8 & 0.4 | 8.96 | 0.1095 | 0.9149 | 2.19 | 0.0123 | 0.9463 | 3796.02 | 544.82 | 1.0051 | 8.23 | 0.1440 | 0.7742 |
| | 1.0 & 0.5 | 8.59 | 0.1722 | 0.6474 | 2.15 | 0.0201 | 0.7587 | 3694.47 | 600.30 | 0.7728 | 8.20 | 0.1862 | 0.7947 |
| 0.01 | 0.2 & 0.1 | 9.52 | 0.0378 | 0.7902 | 2.25 | 0.0040 | 0.7748 | 4099.54 | 305.92 | 0.8422 | 8.32 | 0.0783 | 0.6939 |
| | 0.4 & 0.2 | 9.32 | 0.0773 | 0.9132 | 2.23 | 0.0083 | 0.7865 | 3898.09 | 457.52 | 0.9438 | 8.26 | 0.1193 | 0.9279 |
| | 0.6 & 0.3 | 9.08 | 0.3059 | 0.4922 | 2.20 | 0.3172 | 0.4221 | 3858.47 | 544.80 | 0.5794 | 8.24 | 0.1461 | 0.7041 |
| | 0.8 & 0.4 | 8.84 | 0.3187 | 0.5671 | 2.17 | 0.3167 | 0.4330 | 3741.97 | 617.18 | 0.8101 | 8.21 | 0.1711 | 0.6987 |
| | 1.0 & 0.5 | 8.73 | 0.4107 | 0.6182 | 2.15 | 0.4467 | 0.9187 | 3684.56 | 679.78 | 0.9494 | 8.19 | 0.1855 | 0.6823 |
| 0.25 | 0.2 & 0.1 | 9.28 | 0.1732 | 0.5726 | 2.23 | 0.0187 | 0.5930 | 3987.42 | 491.20 | 0.4163 | 8.28 | 0.1266 | 0.6180 |
| | 0.4 & 0.2 | 8.79 | 0.3421 | 0.6225 | 2.17 | 0.0391 | 0.6009 | 3783.97 | 741.93 | 0.4844 | 8.22 | 0.1981 | 0.9833 |
| | 0.6 & 0.3 | 8.29 | 0.4845 | 0.4432 | 2.11 | 0.0586 | 0.6327 | 3651.09 | 1113.58 | 0.6605 | 8.16 | 0.3169 | 0.5102 |
| | 0.8 & 0.4 | 7.75 | 0.6114 | 0.4663 | 2.04 | 0.0796 | 0.8168 | 3311.33 | 1288.81 | 0.7206 | 8.00 | 0.5099 | 0.7686 |
| | 1.0 & 0.5 | 7.22 | 0.6961 | 0.3969 | 1.97 | 0.0975 | 0.6857 | 2960.14 | 1506.16 | 0.9553 | 7.82 | 0.6783 | 0.9622 |
| 0.50 | 0.2 & 0.1 | 9.15 | 0.2693 | 0.6236 | 2.21 | 0.0295 | 0.3976 | 3817.22 | 493.54 | 0.8011 | 8.01 | 0.1298 | 0.4751 |
| | 0.4 & 0.2 | 8.47 | 0.5681 | 0.9980 | 2.13 | 0.0674 | 0.3489 | 3686.37 | 847.92 | 0.9092 | 8.18 | 0.2393 | 0.9258 |
| | 0.6 & 0.3 | 7.78 | 0.7807 | 0.4362 | 2.05 | 0.1014 | 0.9311 | 3376.59 | 1282.97 | 0.8839 | 8.03 | 0.4494 | 0.7284 |
| | 0.8 & 0.4 | 6.95 | 1.0524 | 0.5317 | 1.93 | 0.1538 | 0.6510 | 2924.68 | 1710.65 | ***1.6059*** | 7.76 | 0.7595 | 0.8469 |
| | 1.0 & 0.5 | 6.16 | 1.0674 | 0.6186 | 1.80 | 0.1766 | 0.8615 | 2437.26 | 1764.62 | **1.9485** | 7.46 | 0.9596 | **1.9743** |
| 1.0 | 0.2 & 0.1 | 9.06 | 0.4003 | 0.4029 | 2.20 | 0.0443 | 0.5398 | 4005.58 | 499.71 | ***1.1855*** | 8.29 | 0.1399 | 0.7926 |
| | 0.4 & 0.2 | 8.18 | 0.8656 | 0.4832 | 2.10 | 0.1076 | 0.8913 | 3616.26 | 927.70 | ***1.0881*** | 8.16 | 0.2504 | ***2.0961*** |
| | 0.6 & 0.3 | 7.24 | 1.1289 | 0.8941 | 1.97 | 0.1705 | 0.4016 | 3277.20 | 1547.20 | ***1.4857*** | 7.98 | 0.5155 | ***1.5631*** |
| | 0.8 & 0.4 | 6.36 | 1.3992 | 0.8159 | 1.83 | 0.2240 | 0.7407 | 2810.84 | 2000.79 | ***2.8865*** | 7.70 | 0.7792 | ***2.1564*** |
| | 1.0 & 0.5 | 5.63 | 1.5982 | 0.5774 | 1.69 | 0.2884 | 0.4133 | 2406.74 | 2003.13 | **2.9553** | 7.38 | 1.0255 | **2.0946** |

Note: Acceptance criterion $D_{\mathrm{n},\alpha,}[1000, 0.01] \leq 1.035$.

## References


Al-Karni, A.A., Al-Shamrani, M.A., 2000. Study of the effect of soil anisotropy on slope stability using method of slices. Comput. Geotech. 26 (2), 83–103. https://doi.org/10.1016/S0266-352X(99)00046-4.

Bishop, A.W., 1955. The use of the slip circle in the stability analysis of earth slopes. Géotechnique 5, 7–17. https://doi.org/10.1680/geot.1955.5.1.7.

Chen, Y.M., Lansivaara, T., Wei, W.B., 2007. Two-dimensional slope stability analysis by limit equilibrium and strength reduction methods. Comput. Geotech. 34, 137–150. https://doi.org/10.1016/j.compgeo.2006.10.011.

Chen, M., Lu, W.X., Zhao, H.Q., Bao, X.H., Jiang, X., 2016. Critical geometric parameters of slope and their sensitivity analysis: a case study in Jilin, Northeast China. Environ. Earth Sci. 75 (832), 1–11. https://doi.org/10.1007/s12665-016-5623-4.

Chen, F.Y., Wang, L., Zhang, W.G., 2019. Reliability assessment on stability of tunnelling perpendicularly beneath an existing tunnel considering spatial variabilities of rock mass properties. Tunn. Undergr. Space Technol. 88, 276–289. https://doi.org/10.1016/j.tust.2019.03.013.

Chen, L.L., Zhang, W.G., Chen, F.Y., Gu, D.M., Wang, L., Wang, Z.Y., 2022. Probabilistic assessment of slope failure considering anisotropic spatial variability of soil properties. Geosci. Front. 13 (3). https://doi.org/10.1016/j.gsf.2022.101371 101371.

Cho, S.E., 2009. Probabilistic assessment of slope stability that considers the spatial variability of soil properties. J. Geotech. Geoenviron. Eng. 136 (7), 975–984. https://doi.org/10.1061/(ASCEGT.1943-5606.0000309.

Chowdhury, R.N., Xu, D.W., 1993. Rational polynomial technique in slope reliability analysis. J. Geotech. Geoenviron. Eng. 119 (12), 1910–1928.

Conover, W.J., 1999. Practical nonparametric statistics. John Wiley & Sons Inc., New York, pp. 145–148.

El-Ramly, H., Morgenstern, N.R., Cruden, D.M., 2002. Probabilistic slope stability analysis for practice. Can. Geotech. J. 39 (3), 665–683. https://doi.org/10.1139/t02-034.

El-Ramly, H., Morgenstem, N.R., Cruden, D.M., 2006. Lodalen slide: a probabilistic assessment. Can. Geotech. J. 43 (9), 956–968. https://doi.org/10.1139/t06-050.

Fenton, G.A., Griffiths, D.V., 2008. Risk assessment in geotechnical engineering. John Wiley & Sons Inc., New York, pp. 177–178.

Griffiths, D.V., Fenton, G.A., 2004. Probabilistic slope stability analysis by finite elements. J. Geotech. Geoenviron. Eng. 130 (5), 507–518. https://doi.org/10.1061/(ASCE)1090-0241(2004)130:5(507).

Griffiths, D.V., Huang, J., Fenton, G., 2009. On the reliability of earth slope in three dimensions. Proc. Royal Soc. A: Math., Phys. Eng. Sci. 465 (2110), 3145–3164. https://doi.org/10.1098/rspa.2009.0165.

Griffiths, D.V., Huang, J.S., Fenton, G.A., 2009. Influence of spatial variability on slope reliability using 2-D random fields. J. Geotech. Geoenvron. Eng. 135 (10), 1367–1378. https://doi.org/10.1061/(ASCE)GT.1943-5606.0000099.

Hassan, A.M., Wolff, T.F., 1999. Search algorithm for minimum reliability index of earth slopes. J. Geotech. Geoenviron. Eng. 125 (4), 301–308. https://doi.org/10.1061/(ASCE)1090-0241(1999)125:4(301).

Hicks, M.A., Chen, J., Spencer, W.A., 2008. Influence Of Spatial Variability On 3D Slope Failures. In: Brebbia, C.A., Beriatos, E. (Eds.), Risk Analysis VI, WIT Transactions on Information and Communication Technologies, 39. WIT Press, Southampton, UK, pp. 335–342. https://doi.org/10.2495/RISK080331.

Hicks, M.A., Nuttal, J.D., Chen, J., 2014. Influence of heterogeneity on 3D slope reliability and failure consequence. Comput. Geotech. 61, 198–208. https://doi.org/10.1016/j.compgeo.2014.05.004.

Hicks, M.A., Spencer, W.A., 2010. Influence of heterogeneity on the reliability and failure of a long 3D slope. Comput. Geotech. 31 (8), 948–955. https://doi.org/10.1016/j.compgeo.2010.08.001.

Huang, J., Lyamin, A.V., Griffiths, D.V., Krabbenhoft, K., Sloan, S.W., 2013. Quantitative risk assessment of landslide by limit analysis and random fields. Comput. Geotech. 53, 60–67.

Hungr, O., 1987. An extension of Bishop's simplified method of slope stability analysis to three dimensions. Géotechnique 37 (1), 113–117. https://doi.org/10.1680/geot.1987.37.1.113.

Janbu, N., Bjerrum, L., Kjaernsli, B., 1956. Soil mechanics applied to some engineering problems. Norwegian Geotech. Inst. Publ. 16, 1–93.

Javankhoshdel, S., Bathurst, R.J., 2016. Influence of cross correlation between soil parameters on probability of failure of simple cohesive and $c$-$\phi$ slopes. Can. Geotech. J. 53 (5), 839–853. https://doi.org/10.1139/cgj-2015-0109.

Kasama, K., Furukawa, Z., Yasufuku, N., 2021a. Cyclic shear property and seismic runout analysis for pumice fall deposit. Soil Dyn. Earthq. Eng. 143. https://doi.org/10.1016/j.soildyn.2021.106588 106588.

Kasama, K., Kurukawa, Z., Hu, L.H., 2021b. Practical reliability analysis for earthquake-induced 3D landslide using stochastic response surface method. Compt. Geotech. 137. https://doi.org/10.1016/j.compgeo.2021.104303 104303.

Kasama, K., Whittle, A.J., 2015. Effect of spatial variability on the slope stability using Random Field Numerical Limit Analyses. Georisk: Assess Manage. Risk Eng. Syst. Geohazards 10, 42–54. https://doi.org/10.1080/17499518.2015.1077973.

Khan, F.S., Malik, A.A., 2013. Probability and sensitivity analysis of slope stability of Naulong dam. Pak. J. Eng. Appl. Sci. 45 (9), 54–64.

Lee, S.W., Ching, J., 2020. Simplified risk assessment for a spatially variable undrained long slope. Comput. Geotech. 117, 103228. https://doi.org/10.1016/j.compgeo.2019.103228.

Li, D.Q., Jiang, S.H., Cao, Z.J., Zhou, W., Zhou, C.B., Zhang, L.M., 2015. A multiple response-surface method for slope reliability analysis considering spatial variability of soil properties. Eng. Geol. 187, 60–72. https://doi.org/10.1016/j.enggeo.2014.12.003.

Li, D.Q., Xiao, T., Cao, Z.J., Phoon, K.K., Zhou, C.B., 2016. Efficient and consistent reliability analysis of soil slope stability using both limit equilibrium analysis and finite element analysis. Appl. Math. Model. 40 (9), 5216–5229. https://doi.org/10.1016/j.apm.2015.11.044.

Liu, S.Y., Shao, L.T., Li, H.J., 2015. Slope stability analysis using the limit equilibrium method and two finite element methods. Comput. Geotech. 63, 291–298. https://doi.org/10.1016/j.compgeo.2014.10.008.

Low, B.K., Lacasse, S., Nadim, F., 2007. Slope reliability analysis accounting for spatial variation. Georisk: Assess Manage. Risk Eng. Syst. Geohazards 1 (4), 177–189. https://doi.org/10.1080/17499510701772089.

Matsuo, M., Kuroda, K., 1974. Probabilistic approach to design of embankments. Soils Found 14, 1–17. https://doi.org/10.3208/sandf1972.14.2_1.

Matthews, C., Farook, Z., Helm, P.R., 2014. Slope stability analysis – limit equilibrium or the finite element method. Ground Eng. 45 (8), 22–28.

Mellah, R., Auvinet, G., Masrouri, F., 2000. Stochastic finite element method applied to non-linear analysis of embankments. Probabilistic Eng. Mech. 15, 251–259. https://doi.org/10.1016/S0266-8920(99)00024-7.

Naylor, D.J., 1982. Finite element and slope stability. Numr. Met. Geotech. 92, 229–244. https://doi.org/10.1007/978-94-009-7895-9_10.

Parker, C., Simon, A., Thorne, C.R., 2008. The effects of variability in bank material properties on riverbank stability: goodwin Creek, Mississippi. Geomorphology 101, 533–543. https://doi.org/10.1016/j.geomorph.2008.02.007.

Phoon, K.K., Kulhawy, F.H., 1999. Characterization of geotechnical variability. Can. Geotech. J. 36 (4), 612–624. https://doi.org/10.1139/t99-038.

Rahardjo, H., Satyanaga, A., Leong, E.C., Ng, Y.S., Pang, H.T.C., 2012. Variability of residual soil properties. Eng. Geol. 141 (19), 124–140. https://doi.org/10.1016/j.enggeo.2012.05.009.

Reid, M.E., Christian, S.B., Brien, D.L., Henderson, S.T., 2015. Scoops3D—software to analyze three-dimensional slope stability throughout a digital landscape. U.S. Geol. Survey Tech. Methods 7–21. https://doi.org/10.3133/tm14A1.

Sivakumar Babu, G.L., Srivastava, A., 2007. Reliability analysis of allowable pressure on shallow foundation using response surface method. Comput. Geotech. 34 (3), 187–194. https://doi.org/10.1016/j.compgeo.2006.11.002.

Stianson, J.R., Fredlund, D.G., Chan, D., 2011. Three-dimensional slope stability based on stresses from a stress-deformation analysis. Can. Geotech. J. 48 (2), 891–904. https://doi.org/10.1139/t11-006.

Suchomel, R., Mašin, D., 2010. Comparison of different probabilistic methods for predicting stability of a slope in spatially variable $c$-$\phi$ soil. Comp. Geotech. 37 (1–2), 132–140. https://doi.org/10.1016/j.compgeo.2009.08.005.

Tabarroki, M., Ahmad, F., Banaki, R., Jha, S.K., Ching, J.Y., 2013. Determining the factors of safety of spatially variable slopes modeled by random fields. J. Geotech. Geoenviron. Eng. 139 (12), 2082–2095. https://doi.org/10.1061/(ASCE)GT.1943-5606.0000955.

Ugai, K., Hosobori, K., 1988. Extension of simplified Bishop method, simplified Janbu method and Spencer's method to three dimensions. Proc. Japan Soc. Civil Eng. 1988 (394), 21–26. https://doi.org/10.2208/jscej.1988.394_21.

Vanmarcke, E.H., 1977. Probabilistic modeling of soil profiles. J. Geotech. Eng. 103 (11), 1227–1246.

Varkey, D., Hicks, M.A., Vardon, P.J., 2017. Influence of Spatial Variability of Shear Strength Parameters on 3D Slope Reliability and Comparison of Analysis Methods. In: Huang, J., Fenton, G.A., Zhang, L., Griffiths, D.V. (Eds.), Geo-Risk 2017 : Impact of Spatial Variability, Probabilistic Site Characterization, and Geohazards, Geotechnical Special Publications, 284. ASCE, pp. 400–409. https://doi.org/10.1061/9780784480717.038.

Wu, X.Z., 2015. Modelling dependence structures of soil shear strength data with bivariate copulas and applications to geotechnical reliability analysis. Soils Found 55 (5), 1243–1258. https://doi.org/10.1016/j.sandf.2015.09.023.

Xiao, T., Li, D.Q., Cao, Z.J., Au, S.K., Phoon, K.K., 2016. Three-dimensional slope reliability and risk assessment using auxiliary random finite element method. Comput. Geotech. 79, 146–158. https://doi.org/10.1016/j.compgeo.2016.05.024.

Yu, H., Salgado, R., Sloan, S.W., Kim, J.M., 1998. Limit analysis versus limit equilibrium for slope stability. J. Geotech. Geoenvron. Eng. 124 (1), 1–11. https://doi.org/10.1061/(ASCE)1090-0241(1998)124:1(1).

Zhang, W.G., Meng, F.S., Chen, F.Y., Liu, H.L., 2021. Effects of spatial variability of weak layer and seismic randomness on rock slope stability and reliability analysis. Soil Dyn. Earthq. Eng. 146. https://doi.org/10.1016/j.soildyn.2021.106735 106735.

Zhang, Z.P., Sheng, Q., Fu, X.D., Zhou, Y.Q., Huang, J.H., Du, Y.X., 2019. An approach to predicting the shear strength of soil-rock mixture based on rock block proportion. Bull. Eng. Geo. Environ. 79, 2423–2437. https://doi.org/10.1007/s10064-019-01658-0.

Zhang, J.Y., Wan, L.P., Duan, G.Y., 2017. Study on sensitivity analysis method of slope stability based on Sweden arc method. Curr. Sci. 113 (11), 2097–2104. https://doi.org/10.1016/j.soildyn.2021.106588.

Zhu, D., Griffiths, D.V., Fenton, G.A., 2019. Worst-case spatial correlation length in probabilistic slope stability analysis. Géotechnique 69 (1), 85–88. https://doi.org/10.1680/jgeot.17.T.050.